Cement and Concrete Composites 173 (2026) 106737

Contents lists available at ScienceDirect

Cement and Concrete Composites

journal homepage: www.elsevier.com/locate/cemconcomp

Influence of fibre treatments on early-age carbonation in yarn-cement paste composites under enforced carbonation

Yixiu Zhuge, Hong S. Wong, Rupert J. Myers *

Centre for Infrastructure Materials, Department of Civil and Environmental Engineering, Imperial College London, London, SW7 2AZ, United Kingdom

ARTICLE INFO

Keywords:
Carbonation curing
Natural fibre
CO2 transport
Hydration
Microstructure

ABSTRACT

This study examines whether yarn moisture state and surface treatment can control CO_2 transport, carbonation extent, and early-age performance in yarn–cement paste composites under enforced carbonation curing. Oven-dried, saturated, cement-slurry-coated, and epoxy-coated jute yarns were embedded in Portland cement paste (w/c = 0.40) and compared with synthetic yarns (acrylic, nylon, and polypropylene). Carbonation was assessed along sample depth using phenolphthalein image analysis, thermogravimetry, quantitative X-ray diffraction, SEM-BSE porosity mapping, and compressive strength testing. Saturated jute yarn produced the most carbonation, forming interconnected carbonated belts due to its porous structure and internal moisture retention, whereas epoxy-coated jute and synthetic yarns showed limited carbonation. Effective carbonation radius correlated strongly with TGA-measured CO_2 uptake ($R^2 = 0.962$) and 24 h water absorption ($R^2 = 0.872$). After 7 days, carbonated cement pastes with 0.76 vol% saturated jute yarn reached compressive strengths of 80.1 MPa, comparable to the cement paste control (77.2 MPa). These results show that simple pre-saturation improves carbonation efficiency, while early-age compressive strength is maintained only at low yarn volume where carbonation-induced densification compensates for fibre-related matrix disruption.

1. Introduction

Cement production contributes 5–8 % of global anthropogenic CO_2 emissions [1,2], primarily from limestone calcination (~60 %) and fossil fuel combustion (~40 %) during clinker formation. While cementitious materials passively reabsorb CO_2 through natural and service-life carbonation, the sequestration rate remains insufficient to neutralise the sector's net emissions. It was recently estimated that 0.84–0.93 Gt CO_2 was absorbed globally in 2023 through carbonation of concrete, mortar, cement paste, and industrial cementitious wastes [3,4]. Cumulative reabsorption of CO_2 since the 1930s is estimated at 21.3–23.9 Gt CO_2 [3,5]. These data show the potential of CO_2 mineralisation in cementitious systems as a viable route to reduce their carbon footprint, particularly when integrated with low-clinker formulations and enforced carbonation [6,7].

Building on this potential, enforced carbonation has been extensively investigated to simultaneously reduce the carbon footprint and enhance the mechanical performance of cement-based materials [8]. The process exploits the reactivity of portlandite with CO_2 dissolved in pore solution, stabilising calcium carbonate phases that densify the microstructure [9]. Under optimised curing regimes, typically involving 10–20 vol% CO_2 [9–11], temperatures of 20–40 °C [12,13], and relative humidity maintained between 50 and 70 % [14–16], rapid reaction occurs during the early stages of hydration when the pore system remains open to gas ingress; excessive moisture restricts gas diffusion, while limited moisture hinders CO_2 dissolution [9,10]. The interplay between hydration and carbonation is therefore critical: hydration consumes water and generates $Ca(OH)_2$ and C-S-H, whereas carbonation depends on that same pore water to dissolve CO_2 and precipitate $CaCO_3$ [9,17,18]. It has been shown that CO_2 exposure within the first 24 h can lower the hydration degree of Portland cement paste (w/c = 0.15, 50 mm × 6 mm discs) by 15–25 % [19], due to early portlandite consumption and $CaCO_3$-induced pore constriction, which impairs ion and moisture mobility. Nonetheless, a synergy between hydration and carbonation has been demonstrated under regulated conditions: Portland cement-fly ash mortars incorporating CO_2-reactive admixtures, such as triethanolamine solutions pre-saturated with CO_2, have shown increased cumulative hydration heat (by 8.6 % at 48 h), reduced total porosity (~20 %) and a shift toward finer pore sizes (100 – 200 nm) [20].

For cement-based materials, laboratory studies report CO_2 uptake

* Corresponding author.
E-mail addresses: yixiu.zhuge20@imperial.ac.uk (Y. Zhuge), hong.wong@imperial.ac.uk (H.S. Wong), r.myers@imperial.ac.uk (R.J. Myers).

https://doi.org/10.1016/j.cemconcomp.2026.106737
Received 21 March 2026; Received in revised form 3 June 2026; Accepted 24 June 2026
Available online 25 June 2026
0958-9465/© 2026 The Author(s). Published by Elsevier Ltd. This is an open access article under the CC BY license (http://creativecommons.org/licenses/by/4.0/).

values of 10–20 wt% of binder mass, with compressive strength improvements of 50–110 % compared with air curing during the first 24–72 h [21–25]. Nevertheless, large-scale commercial applications remain limited by cost and energy constraints [26]. Industrial flue gases containing 15–30 vol% CO_2 are viable curing streams for pre-cast components [6,27,28], yet CO_2 uptake rates remain limited with prolonged curing time [29]. Attempts to overcome poor carbonation efficiency through mix design or curing optimisation, such as cyclic exposure, staged carbonation–hydration curing, or internal water management, have improved efficiency but often compromise mechanical performance [17,19,28,30,31]. Similarly, porosity-engineered approaches using foamed, lightweight, or bio-based additives enhance CO_2 transport but reduce strength [32–34]. These methods enhance CO_2 uptake but often weaken mechanical performance, emphasising the need for alternative designs that maintain both CO_2 transport and strength.

Natural fibres have been incorporated into engineered cementitious composites to enhance mechanical performance and modify gas transport under carbonation curing [35–38]. Fibre bridging limits crack propagation and stabilises the capillary pore network, while the hollow lumens facilitate internal gas transport [39,40], collectively enhancing CO_2 transport under accelerated CO_2 curing. For instance, adding 1 vol % sisal fibre to ECC increased CO_2 uptake by 16 wt% under 99.8 vol% CO_2 at 5 bar for 24 h, attributed to their tubular fibre channels [41]. In parallel, natural fibres can act as internal curing agents by storing and gradually releasing water [42,43]. Cellulose-based fibres, such as flax, hemp, and sisal, can absorb up to 30–40 wt% of their dry mass in water over a period of 7 days, with 10–30 wt% retained as hard-to-remove water that releases after 48 h under ambient exposure [44,45]. At a dosage of 0.3 wt%, cellulose fibres increased hydration heat of high sulphate-resistant cement pastes (w/c = 0.44) by 14 % and reduced early pore connectivity by 72 % at 12 h [46]. In ultra-high-performance concrete (w/b = 0.2) composed of silica fume (25 wt%) and steel fibres (2 wt%), saturated cellulose additions of 1.1 wt% mitigated drying/autogenous shrinkage and improved early cracking control [47]. Fibre surface treatments, typically applied to enhance mechanical bonding, also modify fibre transport behaviour by altering hygroscopicity and interfacial properties: 5 wt% NaOH-treated bamboo fibres reduce water uptake by 15–30 % [48], while silane and acetylation treatments reduce hygroscopicity of bamboo and banana fibres by 40–70 % [49,50]. However, such treatments have not been systematically evaluated for carbonation curing, which could limit the internal curing effect under enforced carbonation conditions.

Spun natural fibre yarns provide a structurally continuous alternative to dispersed short fibres [51]; their aligned filaments and internal lumens provide connected diffusion pathways while retaining moisture for sustained reactions near the fibre–matrix interface. Bast yarns such as jute and hemp show the highest CO_2 uptake and deep carbonation fronts compared with cotton or wool, owing to their porous architecture and moderate compactness [51]. In addition to its superior CO_2 transport capability, jute is the second most produced natural fibre globally after cotton, with an annual output exceeding 3.6 million tonnes and accounting for approximately 80 % of bast fibre production [52]. Unlike seed-derived fibres (e.g. cotton), jute is extracted from the phloem tissue of Corchorus plants and requires minimal fertiliser or pesticide input [53]. As a fast-growing, photoperiod-sensitive crop, 1 ha of jute can absorb up to 15 tonnes of CO_2 and release 11 tonnes of oxygen during its growing season [54]. These combined technical, ecological, and economic characteristics make jute a promising and underutilised reinforcement for low-carbon cement composites [54–57].

Despite these promising attributes, the mechanisms by which yarn moisture state and surface condition control carbonation curing remain insufficiently defined. Previous work showed that natural yarns can enhance CO_2 transport and uptake, but the yarns were used as received, without controlled saturation or surface modification [51]. As a result, the respective roles of internal water retention, fresh-state water redistribution, interfacial pore structure, and fibre–matrix contact could not be separated. It also remains unclear whether treatments that are commonly used to modify natural fibres, such as pre-saturation, cement slurry coating, or polymer sealing, improve or suppress carbonation under early-age CO_2 curing. The interaction between yarn-induced carbonation, hydration, local microstructural development, and early compressive strength therefore requires systematic investigation.

In light of these considerations, this study tests the hypothesis that moisture-retentive jute yarns act as local water reservoirs, sustaining CO_2 dissolution and carbonate precipitation at the yarn–cement paste interface, whereas coatings or synthetic yarns that limit moisture exchange suppress this process. Spun jute yarns were therefore prepared in oven-dried, pre-saturated, cement-slurry-coated, and epoxy-coated states and compared with synthetic yarns under identical enforced carbonation curing. The study first quantifies the effects of yarn moisture state and surface treatment on carbonation geometry and CO_2 uptake, before examining their links with hydration kinetics, phase assemblage, and interfacial microstructure. It then evaluates whether yarn-enhanced carbonation can preserve early-age compressive strength at practical fibre volumes. Phenolphthalein image analysis, thermogravimetric CO_2 quantification, quantitative X-ray diffraction, SEM-BSE porosity mapping, and compressive strength testing are combined to relate carbonation extent, phase evolution, microstructure, and mechanical response.

2. Materials and methods

2.1. Materials

Jute yarns (Tennwell, brown) were the primary natural fibre investigated in this study, based on their promising carbonation performance observed in previous work [51]. As lignocellulosic fibres, jute contains abundant hydroxyl groups and internal lumens [52,55,58], which promote both water uptake and interfacial reactivity in alkaline cementitious environments. To evaluate the effects of moisture state and surface treatments on carbonation and hydration, five jute conditions were prepared (Fig. 1a–e).

Oven-dried jute (ODJ) was conditioned at 60 °C for 24 h to reduce free and loosely bound water, to maximise gaseous transport during carbonation. During drying, the yarn mass was measured every 24 h until the mass change was less than 0.001 g, indicating constant mass under the applied condition. ODJ was therefore used as the low-moisture reference state.

Saturated jute (SJ) was prepared by immersing yarns in deionised water for 24 h, followed by surface blotting to remove external water while retaining internal saturation. These two moisture states were expected to alter the fresh-state water balance around the yarn: ODJ could absorb mixing water from the adjacent paste, whereas SJ acted as a pre-filled water reservoir and imposed a smaller immediate water demand on the surrounding matrix.

Two slurry-coated variants were produced by dip-coating ODJ and SJ in fresh cement slurry (w/c = 0.8). These treatments yielded oven-dried, slurry-coated jute (ODMJ) and saturated, slurry-coated jute (SMJ), respectively, introducing a calcium-rich, high-pH interfacial zone intended to accelerate hydrate formation and local carbonation. Epoxy-coated jute (EJ) was prepared by applying a continuous epoxy layer (resin/hardener ratio 22:3 by mass) to restrict moisture and gas exchange, serving as a wall-effect control to isolate the influence of surface fibre geometry [59].

Three synthetic yarns (Fig. 1f–h) were included as controls to separate the effects of surface chemistry, polarity and moisture uptake typically associated with natural lignocellulosic fibres. Acrylic yarn (Sirdar Double Knitting, green) was selected as a staple-spun fibre with limited chemical reactivity in high-pH cement pore solutions [60]. The yarn could retain a moderate amount of water (Table 1), attributed primarily to capillary retention within the loosely packed fibre bundle

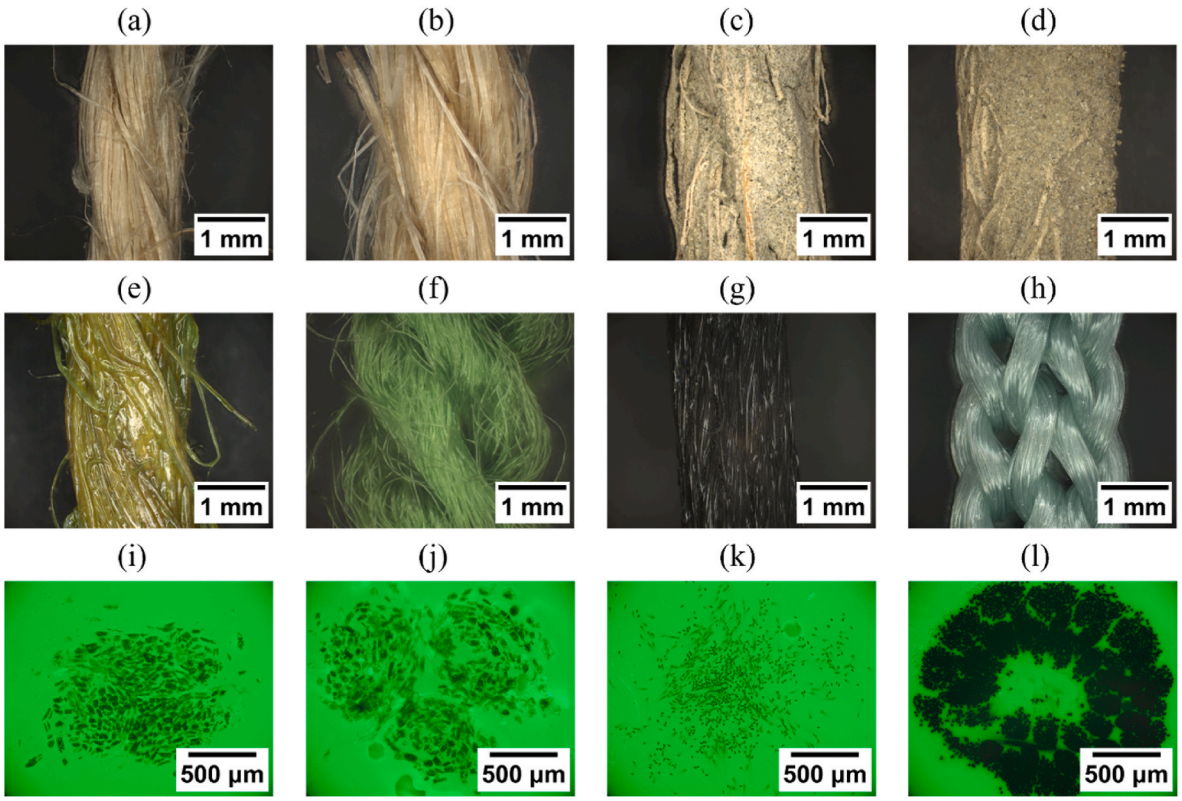


Fig. 1. Representative morphology of the studied yarns. (a–h) Macroscopic appearance of: (a) oven-dried jute (ODJ), (b) water-saturated jute (SJ), (c) oven-dried slurry-coated jute (ODMJ), (d) saturated slurry-coated jute (SMJ), (e) epoxy-coated jute (EJ), (f) acrylic yarn (AC), (g) nylon yarn (N), and (h) polypropylene yarn (P). (i–l) Fluorescence micrographs of transverse sections of yarns embedded in fluorescent epoxy (resin rendered in green; yarn cross-sections appear black): (i) ODJ, (j) SJ, (k) acrylic, and (l) nylon. All micrographs acquired at 10× magnification with identical imaging settings (brightness 46.1 %). (For interpretation of the references to colour in this figure legend, the reader is referred to the Web version of this article.)

Table 1
Properties of the yarns.

Annotation	Fibre type	Treatment	Average diameter – original (mm)	Average diameter – tightened (mm)	Compactness (%)	Water absorption (%)
ODJ	Jute	Oven-dried	1.55 ± 0.0380	1.19 ± 0.0544	48.4	89.6
SJ	Jute	Saturated	2.43 ± 0.0445	2.04 ± 0.0407	39.1	102
ODMJ	Jute	Oven-dried with cement slurry coated	2.27 ± 0.0152	2.16 ± 0.0268	/	56.0
SMJ	Jute	Saturated with cement-slurry coated	2.37 ± 0.0293	2.24 ± 0.0351	/	76.0
EJ	Jute	Epoxy-coated	1.84 ± 0.0342	/	/	7.72
AC	Acrylic	/	2.78 ± 0.0912	0.994 ± 0.0937	13.6	39.5
N	Nylon	/	1.76 ± 0.0156	1.76 ± 0.0154	72.4 %	27.9
P	Polypropylene	/	2.50 ± 0.0208	2.03 ± 0.0767	45.7	19.3

rather than absorption into the polymer. Nylon yarn (Tonifu, black) was chosen as a multifilament polyamide with moderate polarity and water uptake arising from its amide functionality, while remaining chemically stable in alkaline cementitious environments [61]. Polypropylene yarn (Sensy, sage) served as a non-polar, hydrophobic comparator; its chemical inertness and very low surface energy made it a baseline reference for minimal interfacial reactivity [62].

All yarns studied here have a porous structure. Staple-spun yarns such as jute and acrylic contain twist-induced gaps between short fibres, whereas multifilament yarns such as nylon and polypropylene consist of tightly packed filaments with interstitial capillaries [62,63]. To quantify the solid fraction, small yarn segments were vacuum-impregnated with a low-viscosity fluorescent epoxy (resin/hardener ratio 22:3 by mass) and then sectioned and polished for imaging. These images (Fig. 1i–l) were processed to calculate two quantities: the total fibre area (A_f) and the area enclosed by the outer convex boundary of the yarn bundle (A_y). The ratio of these areas is defined as compactness ($C = A_f/A_y$). Compactness was quantified by averaging three cross-sectional measurements per yarn. Coated samples (ODMJ, SMJ, EJ) were excluded from this compactness analysis, as they do not reflect the intrinsic fibre geometry.

Yarn diameters were measured in two conditions: the original diameter, representing the relaxed state, and the tightened diameter, measured under light pretension to simulate placement during casting. Diameters were averaged over 30 positions along each sample to account for local variability from twist and hairiness. Water absorption over 24 h was evaluated following a modified version of BS EN ISO 62:2008 [51,64]. Samples were oven-dried at 60 °C to constant mass, then immersed in deionised water at 23 °C for 24 h. After surface blotting, the saturated mass was recorded and the water absorption (%) was calculated relative to the oven-dry mass. These measured properties are summarised in Table 1.

Yarn-cement paste composites were produced using CEM I 52.5 N Portland cement (Breedon). The chemical composition of the cement, determined by X-ray fluorescence (XRF), is reported in Table 2. A water-to-cement mass ratio of 0.4 was maintained across all samples.

Table 2
Chemical composition of the CEM I 52.5N Portland cement (wt.%). Loss on ignition was 2.01 wt%.

SiO_2	Al_2O_3	Fe_2O_3	CaO	SO_3	MgO	Na_2O	K_2O	Cl^-
19.2	5.44	2.63	63.6	3.30	0.910	0.210	0.530	0.060

2.2. Sample preparation

Two types of cement-paste samples were prepared for characterisation and mechanical testing: (i) 216 cylindrical fibre-centred paste samples cast in centrifuge tubes for cross-sectional and image-based analysis, and (ii) 432 cubes containing mesh-configured yarn arrangements for compressive strength testing.

Cylindrical single-yarn paste samples were cast in 15 ml polyethylene centrifuge tubes using a method adapted from previous work [51]. Prior to casting, each yarn was positioned centrally within the tube by threading it through pre-drilled holes located at the top and bottom ends, and fixed in place externally using waterproof duct tape to maintain alignment (Fig. 2a, steps 1–3). Cement paste was then introduced to fill the tube completely, after which the lid was tightly sealed. With the paste still fresh, longitudinal tension was applied manually to the yarn to maintain straightness and induce mild compaction along the yarn axis. This procedure resulted in a measurable reduction in the average yarn diameter (see Table 1). Tubes were vibrated on a vortex mixer (Fisherbrand) until no air bubbles were visibly escaping (~45 s) and cured in sealed condition for 24 h at ambient temperature. Thereafter, the upper section of each tube was removed using a low-speed precision saw (Buehler IsoMet 1000) under continuous water cooling. Identical samples were prepared in three separate casting batches to ensure repeatability across all measurements.

Cube specimens ($20 \times 20 \times 20\ mm^3$) for compressive strength testing were prepared using a layer-by-layer casting approach (Fig. 2b, steps 1–3) [65]. Yarns were manually placed into the mould, followed by the addition of cement paste to embed the layer. These steps were repeated according to the intended mesh configuration until the mould was filled. The cast specimens were covered with a plastic membrane and cured at >98 % relative humidity for the first 24 h, then demoulded (step 3) and relocated to either air or carbonation curing chambers.

Six mesh configurations were tested to assess the influence of fibre layout on compressive strength (Fig. 2b(i–vi). These varied in the in-plane spacing between yarns (10 mm or 5 mm) and the number of vertical yarn layers (1, 2, or 3 layers). Configurations are labelled using the

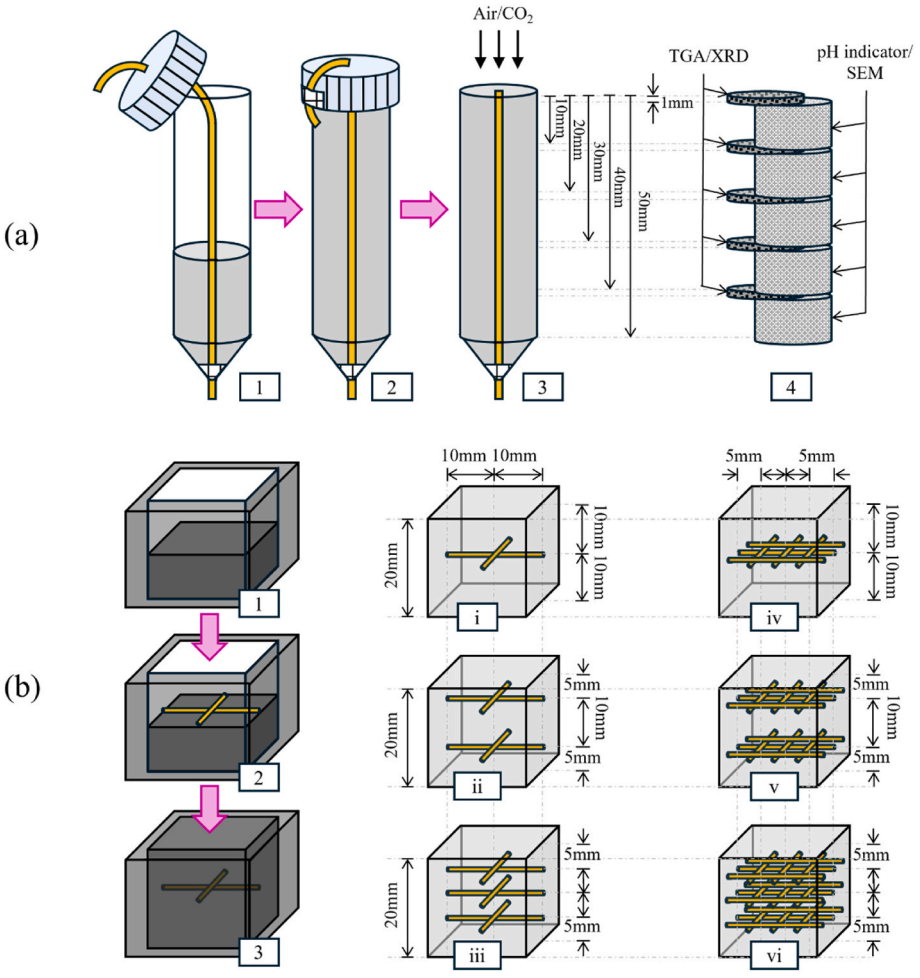


Fig. 2. Schematic diagram of sample preparation. (a) Steps for preparing cylindrical paste samples with a centrally aligned yarn using 15 ml centrifuge tubes: (1) yarn positioned through pre-drilled holes; (2) tube filled with fresh paste and sealed; (3) yarn tensioned longitudinally; (4) top portion removed after curing for cross-sectional analysis. (b) Cube casting sequence and compressive strength specimen configurations: (1–3) paste cast in layers with yarns embedded between lifts; (i–vi) tested arrangements varying in in-plane yarn spacing (10 or 5 mm) and number of vertical yarn layers (1 to 3 layers).

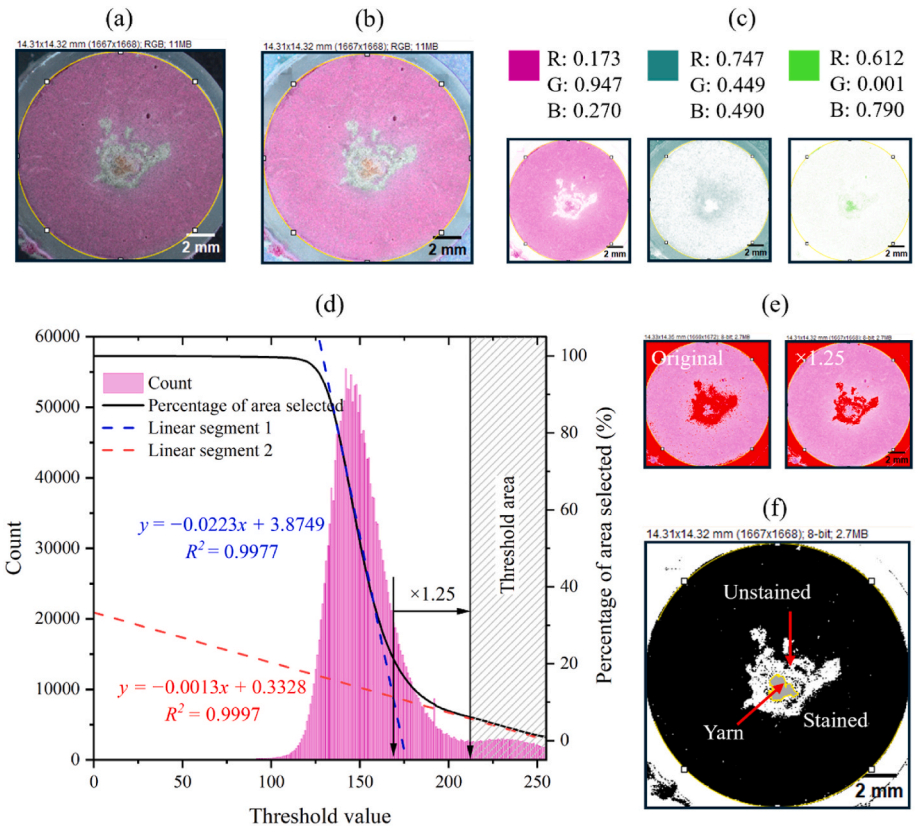


Fig. 3. Image processing workflow for phenolphthalein-stained discs. (a) Raw RGB image with ROI defined. (b) Rolling-ball background subtraction at 100 pixels. (c) Colour deconvolution using standardised vectors: (c-1) phenolphthalein stain; (c-2) cement matrix paste; and (c-3) residual colour. (d) Threshold determination using the overflow segmentation method. (e) Binary mask of carbonated area before and after correction factor (1.25) applied. (f) Schematic illustration of carbonated area fraction. (For interpretation of the references to colour in this figure legend, the reader is referred to the Web version of this article.)

format X–YL, where X denotes the xy-plane spacing in mm, and Y indicates the number of layers (e.g., 10–3L represents 3 stacked yarn layers with 10 mm in-plane spacing). Two additional configurations with 2.5 mm spacing were tested for completeness and are reported in the Supporting Information; these were unsuccessful due to their excessive fibre content that hindered paste placement and compaction.

2.3. Curing procedure

After the upper sections of tubes were removed, the cylindrical samples were fan-dried for 30 min at ambient conditions (21 ± 2 °C; 55 ± 5 % RH) using a bench-top electric fan, to promote evaporation of free water from the freshly cut surface. After drying, cylindrical samples were transferred to a Panasonic MCO-230AIC CO_2 incubator and positioned upright on a centrifuge stand, leaving only the top surface exposed. Enforced carbonation was conducted under conditions approximating cement plant flue gas: 19.9 ± 0.1 vol% CO_2 (prepared by mixing compressed air with 99.8 vol% CO_2 from BOC Ltd), 25 ± 0.5 °C, and ambient atmospheric pressure. Relative humidity was regulated at 64 ± 2 % using a saturated $NaNO_2$ solution placed inside the chamber. Samples were exposed to CO_2 for 1, 3, 5, or 7 days, then retrieved in batches for analysis.

To enable comparison with CO_2-cured specimens, a parallel set of samples was prepared and air-cured under identical time frames. These control samples were stored in a climate chamber regulated by saturated sodium nitrite solution (21 ± 2 °C, 64 ± 2 % RH) for 1–7 days.

Post-curing, all cylindrical specimens were sectioned for characterisation tests using a Buehler IsoMet 1000 low-speed precision saw (Fig. 2a, step 4). For each 10 mm-thick cylindrical disc, the uppermost 1 mm was reserved for thermogravimetric analysis (TGA) and X-ray diffraction (XRD). These discs were immediately hand-ground under isopropanol using an agate mortar, and subjected to solvent exchange to stop hydration [66]. Samples were then stored under low vacuum (0.2 bar) over silica gel and granular soda lime (Thermo Scientific) to minimise further carbonation. The remaining 9 mm-thick disc was first sprayed with a phenolphthalein pH indicator and imaged for carbonated area fraction, then subsequently used for SEM sample preparation. All characterisation and mechanical testing in this study was conducted immediately following the specified curing durations, with no additional ageing or post-curing applied prior to testing.

Disc samples are labelled as [Fibre]–[Curing]–D[Day]–[Depth], Curing = C (carbonated) or A (air-cured), D[Day] denotes the curing duration, and Depth is the sampling depth in mm. For example, SJ–C–D7–10 refers to a saturated jute yarn-cement disc, carbonation-cured for 7 days, with measurements taken at 10 mm from the exposed surface.

2.4. Image analysis

2.4.1. Phenolphthalein indicator test

Carbonation fronts on cross-sectional discs in Fig. 2a (step 4) were revealed by spraying phenolphthalein (10 g in 1 L of a 50 vol% ethanol–water solution), in accordance with BS EN 12390-12:2020 [67]. After the stain stabilised, colour images were acquired using an Olympus SZX-10 stereomicroscope with an SC50 CMOS camera under oblique fibre-optic illumination (Highlight 3000). Imaging parameters were held constant (normal light intensity, brightness 2.5, exposure 150 ms). Samples were placed on a black motorised XY stage; a ruler was placed at the focal plane to verify scale.

Image processing was carried out using ImageJ 1.54p with a custom

Table 3
Validation of overflow-based image segmentation against manual segmentation for different threshold correction factors. Agreement is quantified for the carbonated area fraction using mean absolute error (MAE), standard error (SE) of error, and coefficient of determination. Threshold values correspond to the lower bounds applied to the deconvoluted binary images.

Correction factor	Threshold	$f_{carbonated}$			$r_{carbonated}$		
		MAE (%)	SE of error (%)	r^2_{manual}	MAE (mm)	SE of error (mm)	r^2_{manual}
1.00	168	10.8	2.22	0.937	1.19	0.17	0.920
1.10	185	4.07	0.84	0.991	0.54	0.08	0.982
1.20	201	1.34	0.35	0.998	0.21	0.05	0.993
1.25	210	0.99	0.21	0.999	0.14	0.03	0.994
1.30	218	1.60	0.38	0.999	0.18	0.03	0.993
1.40	235	6.09	1.71	0.995	0.53	0.08	0.984

macro to automate batch analysis (Supporting Information S1, Section S1). A circular region of interest (ROI) was defined to isolate the paste interior and exclude the centrifuge tube rim (Fig. 3a). To remove uneven lighting and reduce background interference, a rolling-ball background subtraction (radius: 100 pixels, light background, Fig. 3b) was applied, improving on the method proposed by Zhuge et al. [51] by increasing the contrast of local grey tones and reducing the effects of lighting artefacts. Colour deconvolution was then applied to separate the phenolphthalein-stained region from the cement matrix using a single set of colour vectors applied across all 540 discs (Fig. 3c). These vectors were averaged from 10 reference images of (i) phenolphthalein-stained, uncarbonated cement paste, and (ii) unstained paste. The third channel (residual) appeared nearly blank, except for yarn features, and was used to mask yarn areas from analysis.

To segment the carbonated area, the threshold was determined using a modified overflow segmentation approach (Fig. 3d, Table 3) [52]. Pixel-intensity histograms were analysed using lines tangential to the inflection point and flat region of the high-intensity part of the cumulative area fraction curve (Fig. 3d); their intersection was used as the base threshold [68]. As overflow segmentation systematically tended to overestimate the carbonated region, the threshold derived from the cumulative histogram was scaled by a correction factor prior to binarisation (Fig. 3e). Based on the processed images, carbonated area fraction ($f_{carbonated}$, %) was computed as the percentage of unstained area within the ROI, excluding yarns (Fig. 3f, Eq. (1)). To normalise for variations in sample size and yarn cross-section, the effective carbonation radius ($r_{carbonated}$, mm) was also calculated (Eq. (2)). This metric reflects the equivalent radial penetration depth of carbonation and allows comparison across samples with different fibre sizes or disc diameters. The results were used to select representative samples for further characterisation tests.

$$f_{carbonated} = \frac{A_c}{A_{ROI} - A_f} \times 100 \quad (1)$$

$$r_{carbonated} = \sqrt{\frac{A_c}{\pi}} - \sqrt{\frac{A_f}{\pi}} \quad (2)$$

Where A_{ROI} is the region of interest, A_f is the yarn area. A_c represents the threshold carbonated area (Fig. 3e).

The correction factor was selected by systematic comparison of automated segmentations with manual delineation of the carbonation boundary on a representative subset of 20 discs containing SJ, ODJ, ODMJ and EJ composites after 7 days of carbonation (Supporting information Section S1, Fig. S1). Correction factors in the range 1.00–1.40 were evaluated. As summarised in Table 3, a correction factor of 1.25 produced the smallest mean error and the highest agreement with manual segmentation for both the carbonated area fraction and effective carbonation radius ($r^2 > 0.99$). This correction factor was therefore adopted for all subsequent image analyses.

2.4.2. Scanning electron microscopy

SEM was used to investigate the microstructural evolution and porosity characteristics of selected fibre-reinforced cement pastes following 7 days of either air or carbonation curing. SEM samples were prepared from the same discs used for phenolphthalein analysis. After image acquisition, the remaining 9 mm disc segments were submerged in isopropanol for 72 h to halt hydration, following the standard solvent exchange protocol [69]. Samples were dried in a 40 °C oven until constant mass before epoxy impregnation. Samples were vacuum-impregnated with low-viscosity epoxy resin and placed in a high-pressure chamber at 2.5 bar for 24 h. Impregnated specimens were then sectioned, polished, and carbon-coated (15 nm) using an Emitech K550X sputter coater under a vacuum of 7×10^{-2} mbar.

The extracted discs were imaged at 1 mm, 11 mm, 21 mm, 31 mm, and 41 mm depths (Fig. 2a, step 4). Backscattered electron (BSE) imaging was performed using a Zeiss Sigma 500VP field emission SEM equipped with a 5-quadrant high-definition BSE detector. Images were acquired at 15 kV accelerating voltage, 8.5 mm working distance, and a resolution of 1024 × 768 pixels. All images were captured at 500× magnification under fixed brightness (45 %) and contrast (43 %) settings to allow comparisons.

Each SEM disc comprised a single transverse cross-section of the composite, within which four regions of interest were defined: (i) the yarn cross-section, (ii) the interfacial transition zone (ITZ) adjacent to the yarn, (iii) the intermediate matrix region, and (iv) matrix at the edge of the samples. For each region, 30 BSE images were acquired and averaged to obtain representative porosity values, yielding 120 images per disc. In total, porosity analysis was based on approximately 3600 SEM–BSE images.

Porosity quantification was performed using the overflow segmentation method [68], which represents the original form of the approach adapted earlier for image analysis (Section 2.5). Here, pixel-intensity histograms from each BSE image were fitted with two linear shoulders, and their intersection, corresponding to the upper intensity threshold, was used to segment pores (dark regions) from the solid matrix. Pore area fractions (μ_p) were calculated as the ratio of segmented pore area to total image area.

2.5. Characterisation test

2.5.1. Isothermal conductivity calorimetry

Isothermal calorimetry was conducted on selected paste samples to assess the influence of fibre type and moisture state on hydration kinetics, following the procedure outlined in BS EN 196-11:2018 [70]. Cement paste was prepared at w/c = 0.40 using the same Portland cement as the composite specimens. The cement powder and water were first mixed using a mini-vortex mixer for 2 min, followed by 30 s of manual mixing to improve paste homogeneity. The fresh paste was then transferred into a calorimetry ampoule, after which 30 mm segment of yarn was added and fully submerged in the paste. The ampoule was sealed immediately after preparation and placed in the calorimeter. Heat flow was recorded continuously over 7 days, and cumulative heat release was normalised to the cement mass. A paste-only sample was tested as the reference.

2.5.2. Thermogravimetric analysis

Thermogravimetric analysis (TGA) was used to quantify portlandite consumption and calcium carbonate formation during curing. As shown in Fig. 2a , 1-mm-thick discs were collected at 10 mm intervals, crushed, and sieved to <125 μm. Approximately 55 ± 0.1 mg of powder was analysed using a Netzsch STA 449 F5 thermal analyser, heated from 30 °C to 1050 °C at 10 °C/min under nitrogen flow (50 ml/min).

Mass losses corresponding to portlandite and $CaCO_3$ were quantified using the tangential method [69], with decomposition ranges defined as 420–520 °C and 550–850 °C, respectively. These intervals were determined based on previous TGA–MS work on carbonated yarn–cement paste composites [51]. Results were expressed as weight percentages relative to the initial cement mass. The total CO_2 uptake (wt.%) was calculated by subtracting the mass of pre-existing CO_2 in the cement from the total $CaCO_3$-derived mass loss. The origin anhydrous cement mass (M_{cement},g) was obtained as the residual mass after heating to 1050 °C (M_{1050}), combined with the mass loss of $CaCO_3$ of the raw cement (Eq. (3)). CO_2 uptake (U_{CO_2}, wt.%) was then calculated using Eq. (4). To distinguish carbonation-induced phase changes from hydration alone, a parallel series of air-cured specimens was analysed at identical curing durations.

$$M_{cement} = \frac{M_{1050}}{1 - \frac{CO_{2,initial}}{100}} \tag{3}$$

$$U_{CO_2} = \frac{M_{CaCO_3} - CO_{2,initial} \times M_{cement}}{M_{cement}} \times 100 \tag{4}$$

Where M_{CaCO_3} (g) is the mass loss from $CaCO_3$ decomposition, and $CO_{2,initial}$ (wt.%) is the percentage of CO_2 initially present in cement as determined by TGA (1.78 ± 0.25 wt%). This normalisation accounts for both crystalline and amorphous carbonates that may decompose below 600 °C.

2.5.3. Quantitative X-ray diffraction

X-ray diffraction (XRD) was used to complement TGA by enabling phase-specific identification of crystalline hydration, carbonation, and residual clinker phases. Measurements were conducted using a Bruker AXS D8 Advance diffractometer with Cu Kα radiation, operated at 45 kV and 40 mA. Powdered samples were collected from 5 depths (0–1 mm, 10–11 mm, etc; see Figs. 2a–4), homogenised, and sieved to <63 μm. Quantitative XRD was performed via Rietveld refinement, using 20 wt% corundum (Al_2O_3) as an internal standard. Data were processed in HighScore Plus software using the ICDD PDF-4+/Web 2023 database. Full details of the analytical procedure are provided in the Supporting Information S1 (Section S3).

To quantify the relationship between hydration and carbonation, a carbonation-to-hydration ratio was introduced (Eq. (5)).

$$Carbonation \quad to \quad hydration \; ratio = \frac{\frac{w_{CaCO_3}}{M_{CaCO_3}}}{\frac{w_{CaCO_3}}{M_{CaCO_3}} + \frac{w_{Ca(OH)_2}}{M_{Ca(OH)_2}}} \tag{5}$$

Where w_{CaCO_3} and $w_{Ca(OH)_2}$ are the Rietveld-refined fractions (wt.%) of calcium carbonates and portlandite, where initial $CaCO_3$ in raw cement was excluded from calculation to isolate carbonation-derived phases. M_{CaCO_3} and $M_{Ca(OH)_2}$ are the molar masses, correspondingly. A higher carbonation to hydration ratio indicates a larger fraction of the measured Ca-bearing reaction products present as carbonate rather than residual portlandite.

2.6. Compressive strength test

Compressive strength was determined on 20 mm cube specimens to

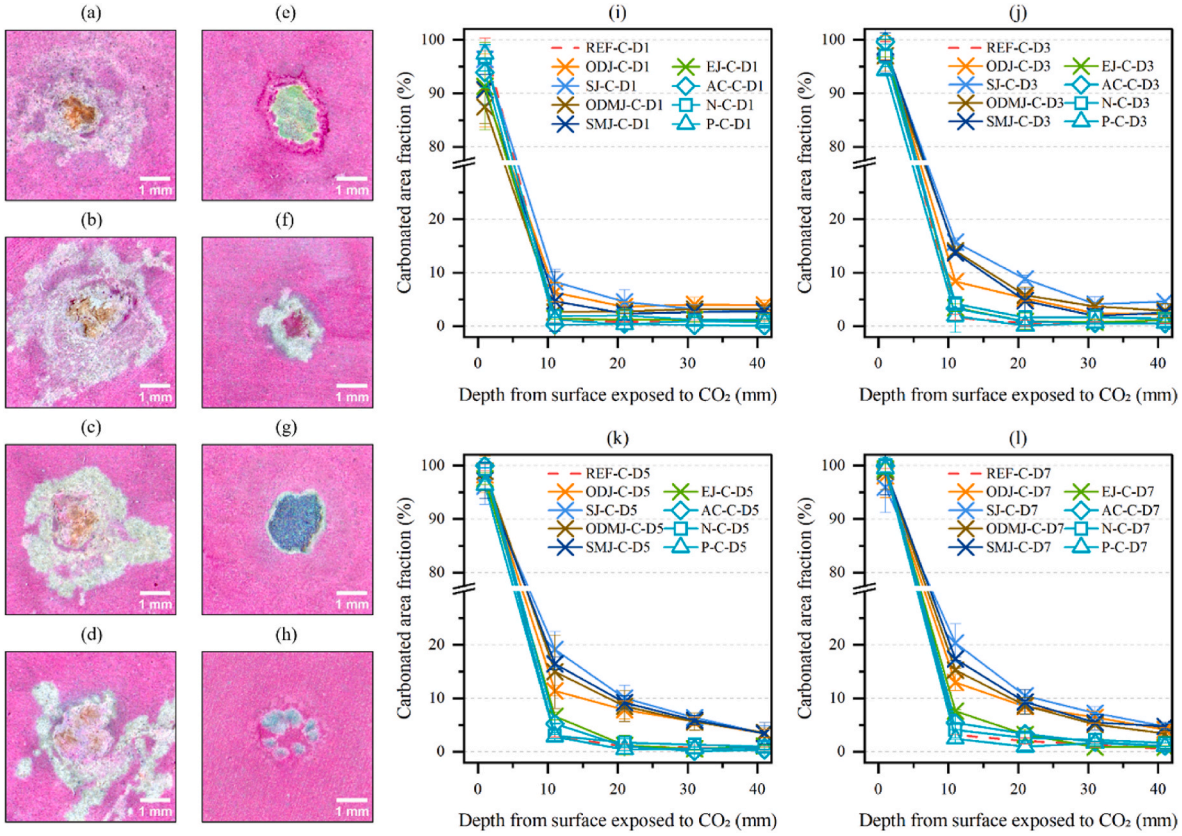


Fig. 4. Carbonation front geometry and quantitative carbonation assessments. (a–h) Stereomicrographs of phenolphthalein-stained disc cross-sections at 20 mm depth after 7 days enforced carbonation: (a) ODJ, (b) SJ, (c) ODMJ, (d) SMJ, (e) EJ, (f) acrylic, (g) nylon and (h) polypropylene. (i–l) Carbonated area fractions from 0 to 40 mm depth measured at different curing durations: (i) 1 day, (j) 3 days, (k) 5 days, and (l) 7 days.

assess the mechanical performance of yarn-cement paste composites under both air curing and enforced carbonation. Six yarn configurations were tested, as illustrated in Fig. 2b, covering different yarn spacings and layer numbers. The yarn replacement level was calculated as the yarn volume fraction within each specimen, based on the convex cross-sectional area of the yarn (measured from image analysis) multiplied by the total embedded yarn length for each mesh configuration.

Compressive strength testing was carried out using an Instron 6800 series universal testing machine equipped with Bluehill Universal software for load control and data acquisition. The load was applied at a constant crosshead displacement rate of 0.5 mm/min until failure. For each configuration and curing regime, 3 replicate cubes were tested, and the mean strength was reported.

3. Results and analysis

3.1. Carbonated area fraction and CO_2 uptake

The stereomicrographs in Fig. 4a–h presents cross-sections of phenolphthalein-stained specimens that have been carbonation-cured for 7 days and extracted at a depth of 20 mm from the exposed surface. These images highlight the variability in carbonation front geometry due to difference in fibre type and surface treatment, which was observed in all samples. Among the jute-based cement composites, uncoated jute yarns (ODJ and SJ) and cement slurry-coated yarns (ODMJ and SMJ) induce irregular, asymmetric carbonation belts encircling the centre. These belt-shaped carbonation regions are characteristic of bast yarn–cement paste composites [51], where twisted yarn geometry promotes localised gas–liquid interaction.

The SJ composite (Fig. 4b) exhibited a broader carbonation belt than ODJ (Fig. 4a), whereas slurry-coated jute composites (Fig. 4c and d) showed sharper and more confined fronts. This indicates that the cement slurry coating restricted lateral spread while creating a locally alkaline region that favoured carbonation close to the yarn. By contrast, epoxy-coated jute (EJ; Fig. 4e) showed no visible carbonation belt at this depth, indicating that the epoxy barrier inhibited moisture and CO_2 exchange across the fibre–cement paste interface. The hydrophobic epoxy surface may also have reduced wetting by the fresh pore solution, further limiting interfacial hydration and carbonation reactions.

Synthetic yarn composites (Fig. 4f–h) showed much smaller carbonation fronts, largely confined to the immediate yarn vicinity. This behaviour is consistent with their lower water sorption (Table 1) and weaker influence on local moisture distribution. Acrylic produced a modest localised rim, likely due to capillary retention within its staple-spun bundle, while nylon showed a smaller, compact rim consistent with its dense multifilament structure. Polypropylene produced no observable carbonation belt, in line with its hydrophobic and non-polar surface.

The carbonated area fraction profiles in Fig. 4i–l shows that carbonation progressed rapidly during the first 3 days and then approached a transport-limited regime. At Day 1, carbonation was mainly confined to the near-surface region (<15 mm). By Day 3, the carbonated area fraction at 11 mm reached ~16 % for SJ and ~14 % for slurry-coated jute, compared with ~8 % for ODJ. Further exposure from 5 to 7 days produced only minor increases (<2 %). Across all depths, SJ consistently showed the largest carbonated area fractions, followed by slurry-coated and oven-dried jute, whereas EJ and synthetic-yarn composites remained weakly carbonated (<8 %). These results indicate that moisture-retentive yarns promote deeper and more extensive carbonation than low-moisture or moisture-blocked yarn systems.

Overall, jute-based composites showed substantially higher carbonation extents than synthetic-yarn composites under the present curing conditions. Carbonated area fractions in jute systems were typically 3–5 times higher than those in acrylic, nylon, or polypropylene composites, consistent with their higher water absorption and more open, moisture-retentive yarn structures. The close agreement between carbonated area fraction and 24 h water absorption (Table 1) indicates that yarns capable of retaining more moisture sustained CO_2 dissolution and carbonation reactions in the adjacent matrix more effectively.

3.2. Heat of hydration and phase assemblages

Fig. 5 shows the normalised heat flow and cumulative heat release profiles for pastes containing oven-dried and pre-saturated yarns. All samples exhibited a single dominant hydration peak between 6 and 10 h, typical of C_3S hydration. Minor variations were observed: saturated jute (SJ) and saturated acrylic (SA) produced slightly broader and delayed peaks, with marginally higher cumulative heat (~304 J/g) than their oven-dried counterparts (~295 J/g). However, these differences were within 3 %, indicating that fibre type and moisture state had only a minor influence on bulk hydration kinetics over 7 days. Therefore, the enhanced carbonation observed in natural-fibre cement paste composites cannot be attributed to accelerated bulk hydration. Under the applied CO_2 concentration and curing humidity, hydration was likely limited relative to sealed or high-humidity curing; differences in carbonation behaviour are more plausibly associated with local moisture distribution and yarn-adjacent pore structure.

Representative thermogravimetric (TG) and derivative thermogravimetric (DTG) curves for the 7-day carbonation-cured saturated jute (SJ) composite are shown in Fig. 6a. Distinct reductions in portlandite decomposition (420–520 °C) were consistent with increasing mass losses between 550 and 850 °C, confirming extensive carbonation. The DTG curves exhibits a distinctive double-shoulder feature: the first shoulder (~550–770 °C) is attributed to poorly crystalline and metastable carbonate phases, including vaterite or aragonite [71], amorphous $CaCO_3$, as well as carbonates formed through C–S–H decalcification and carbonation. These carbonates may be finely dispersed within the decalcified silicate gel and therefore decompose at lower temperatures than well-crystallised calcite. The sharper peak between 770 and 850 °C corresponds to well-crystallised calcite, the dominant carbonation product. At the surface directly exposed to CO_2, decomposition onset is visible as early as 400–450 °C, suggesting the presence of amorphous or highly disordered $CaCO_3$, potentially associated with carbonated C–S–H or finely dispersed amorphous $CaCO_3$ [72]. This multi-peak behaviour reflects the coexistence of metastable and stable carbonate phases formed under varying local conditions of pH and CO_2 concentration. Such phase diversity is consistent with literature that all three polymorphs can form when the ambient relative humidity ranges between 20 % and 80 % [73]. The full TG–DTG curves for both air- and carbonation-cured specimens at 1 and 7 days are provided in the Supporting Information (Section S2, Fig. S2).

Quantified $CaCO_3$ and $Ca(OH)_2$ contents obtained from TGA for the reference paste, ODJ- and SJ-embedded systems after 7 days of carbonation curing are shown in Fig. 6b and c. Carbonation curing led to marked portlandite depletion across all depths, accompanied by proportional carbonate accumulation. Saturated jute (SJ) composites recorded the highest $CaCO_3$ contents throughout the profile, followed by oven-dried jute, while reference paste exhibited limited carbonation. These trends confirm that the extent of carbonation scales with fibre moisture-retention capacity, consistent with image-based analyses. A strong linear correlation was observed between CO_2 uptake and effective carbonation radius for the selected reference paste, ODJ, and SJ specimens after 7 days of carbonation curing across the analysed depths ($R^2 = 0.962$, Fig. 6d). This indicates that, although phenolphthalein staining is pH-based, the effective carbonation radius provides a useful comparative indicator of carbonation extent for the tested systems. For yarn systems where TGA was not performed, CO_2 uptake was estimated from this linear relationship using the corresponding image-derived effective carbonation radius and is shown as filled blue markers in Fig. 6d. At 10 mm depth, the effective carbonation radius around individual yarns was approximately 2–3 mm, which was used to define the minimum yarn spacing in mesh arrangements (Section 3.4) to avoid

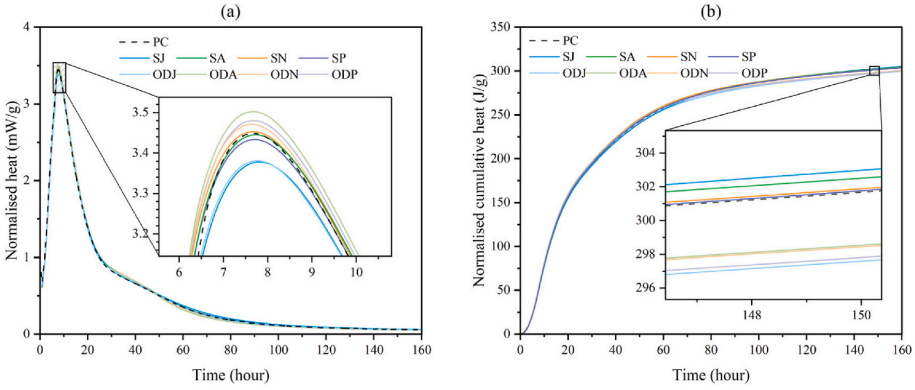


Fig. 5. Isothermal conduction calorimetry results for pastes containing oven-dried (ODJ, ODN, ODA, ODP) and saturated (SJ, SN, SA, SP) yarns, alongside a paste control (PC). (a) Normalised heat flow curves over 7 days. (b) Normalised cumulative heat release over 7 days.

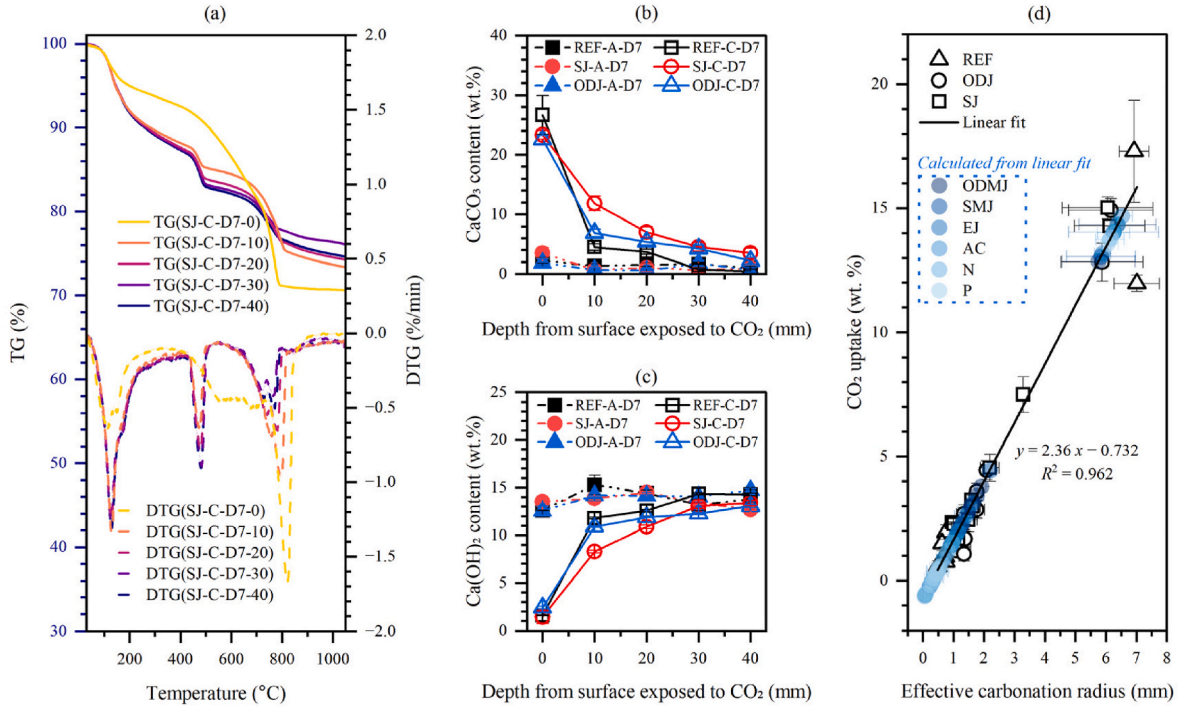


Fig. 6. Thermogravimetric analysis of yarn–embedded cement paste dicsc. (a) TG–DTG curves of saturated jute (SJ) after 7 days of carbonation. (b-c): Depth profiles of (b) $CaCO_3$ contents after 7 days; (c) corresponding $Ca(OH)_2$ contents. (d) Linear correlation between CO_2 uptake and effective carbonation radius. Open symbols denote TGA-measured CO_2 uptake, while filled blue symbols denote values calculated from this linear fit using image-derived effective carbonation radius. The dashed blue box highlights these calculated data points. (For interpretation of the references to colour in this figure legend, the reader is referred to the Web version of this article.)

overlapping carbonation zones.

To complement the thermogravimetric results, quantitative XRD was conducted to assess the relative progression of carbonation and hydration reactions (Fig. 7). As shown in Fig. 6a, the XRD patterns of the saturated jute composite after 7 days of enforced carbonation reveal the presence of portlandite (CH), ettringite, calcite, vaterite, and residual unhydrated clinker phases such as alite (C_3S) and belite (C_2S). Calcite dominated the crystalline carbonate phases, while vaterite was present only in small quantities. Therefore, the low-temperature shoulders in the DTG curves (Fig. 6a) cannot be attributed solely to crystalline vaterite [71]. They are also likely to include amorphous or poorly crystalline carbonate species formed during C–S–H decalcification, which are not resolved by XRD. This interpretation is consistent with the broad DTG response at lower temperature and the limited crystalline vaterite detected by XRD.

At the exposed surface (0–1 mm), all carbonation-cured samples exhibit carbonation-to-hydration ratios approaching unity (Fig. 7b), indicating extensive portlandite depletion and carbonate formation near the CO_2-exposed surface. With increasing depth, the index decreased progressively, reflecting the transition from carbonation-dominated to hydration-dominated phase assemblages. The decline was slower in SJ, which maintained a higher index at 10 mm than ODJ, nylon, and the reference paste. This indicates that moisture retained in SJ sustained carbonation reactions beyond the near-surface zone at early ages. At greater depths (>20 mm), all carbonation-cured systems converged towards similarly low index values, consistent with the effective carbonation radius derived from image analysis. Detailed phase assemblages are provided in the Supporting Information (Section S3, Fig. S3). These results corroborate the TGA analysis, confirming that moisture-retentive natural fibres promote greater portlandite consumption and carbonate

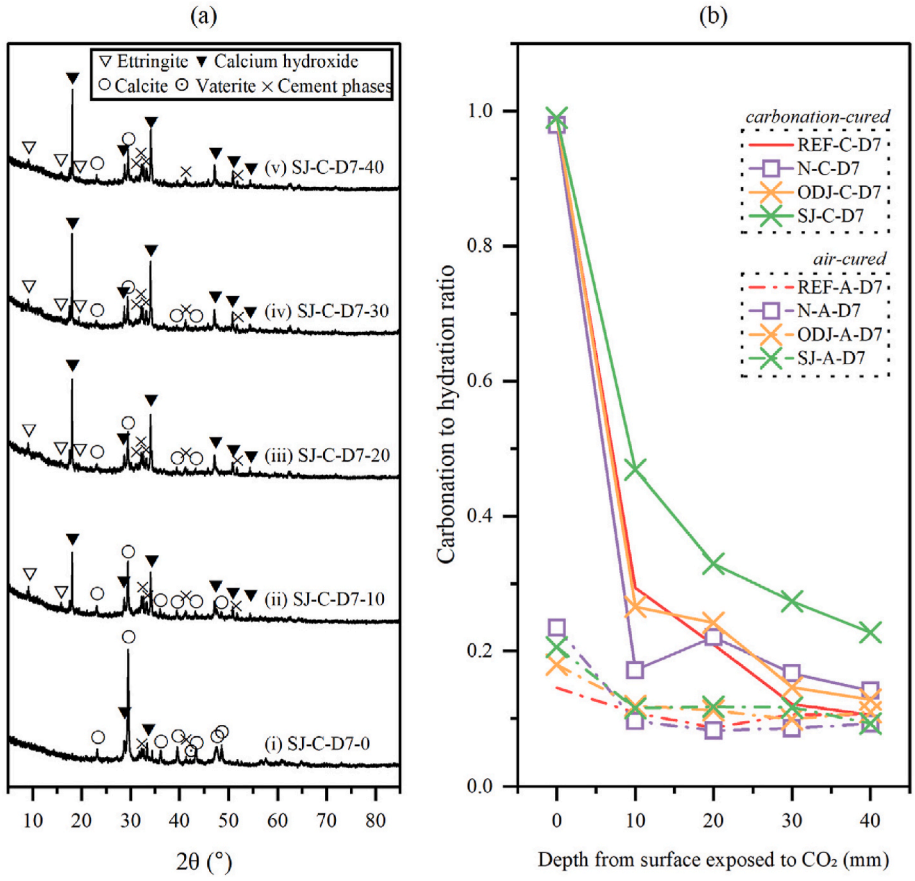


Fig. 7. (a) XRD patterns of saturated jute–cement discs after 7 days of enforced carbonation, sampled from 0 to 40 mm depths; cement phases include alite, belite, tricalcium aluminate, and tetracalcium aluminoferrite. (b) Carbonation-to-hydration ratios of yarn–cement discs after 7 days of curing.

formation within the carbonated zone.

3.3. Microstructure of carbonated yarn-cement paste composites

To contextualise the transformations induced by carbonation, the microstructures of early-age air-cured composites are first presented in Fig. S5 (Supporting Information, Section S5). Under sealed curing, the interfacial transition zone (ITZ) porosity ranged from ~32 % in oven-dried jute (ODJ) to ~21 % in saturated jute (SJ), and ~18 % in nylon composites. ODJ absorbs mixing water from the paste, locally lowers effective w/c near the yarn, causes fibre swelling/shrinkage and poorer packing, whereas SJ does not draw water from the fresh paste and therefore gives a better-filled ITZ. SJ also formed a narrower and more continuous ITZ, while the porous middle rim was diffuse in SJ, sharply banded in ODJ, and largely absent in nylon. These baseline differences govern subsequent microstructural evolution under carbonation.

Carbonation curing induced distinct microstructural transformations in all yarn–cement paste systems, most prominently in jute composites. SEM-BSE analysis of 7-day carbonated specimens (Fig. 8, a1,b1) reveals modified zones analogous to those observed under air curing (Fig. S5), but with more clearly defined zone boundaries and densification effects. Four characteristic zones are consistently observed: (I) the yarn cross-section; (II) a densified interfacial transition zone (ITZ); (III) a partially carbonated matrix belt; and (IV) uncarbonated bulk matrix. These match the optical carbonation front geometries in phenolphthalein-stained samples (Fig. 4). Detailed porosity profiles and radial schematics for each system are provided in Fig. S5 (Supporting Information, Section S4).

Within the yarns (Zone I), the internal morphology of the yarns remained stable after 7 days of enforced carbonation. Both oven-dried (Fig. 8, a2) and saturated jute fibres (Fig. 8, b2) showed no visible degradation or delamination. Saturated jute retained well-defined lumens and high porosity ($\mu_p = 48.6$ %), whereas oven-dried jute showed partially collapsed bundles with slightly lower porosity ($\mu_p = 42.9$ %). Nylon bundles (Fig. 8, c1) remained dense and compact ($\mu_p = 13.1$ %), with no observable structural change relative to their air-cured counterparts.

At the fibre–matrix interface (Fig. 8, Zone II), carbonation markedly densified the ITZ in all cement paste composites, with the extent dependent on yarn type and moisture condition. In ODJ-C-D7 (Fig. 8, a3), ITZ porosity decreased from 32.3 % to 15.5 %, a 52 % reduction relative to air curing, accompanied by brighter BSE contrast indicative of $CaCO_3$ precipitation. In SJ-C-D7 (Fig. 8, b3), the ITZ became even denser ($\mu_p = 10.5$ %), appearing as a carbonate-rich interfacial rim with sharply defined boundaries in the examined cross-sections. Nylon (Fig. 8, c1) exhibited only moderate densification ($\mu_p = 13.1$ %, −26 % relative to air-cured), suggesting more limited microstructural modification.

The porous middle rims surrounding the ITZ (Fig. 8, Zone III) evolved differently depending on fibre type. In ODJ composites (Fig. 8, a4), carbonation slightly reduced porosity from 16.8 % to 14.0 % (−16 %), while rim thickness remained similar (0.74–0.38 mm). SJ composites (Fig. 8, b4) developed a broader and more homogeneous middle rim extending up to 1.20 mm from the yarn, with porosity decreasing to 15–17 % and fewer sharply defined porous belts. This suggests that CO_2 penetration was more spatially uniform around saturated fibres in the examined sections, consistent with moisture-assisted transport near the yarn. Nylon composites (Fig. 8, c2) displayed only minor changes, with the middle rim remaining narrow (~0.7 mm) and porosity largely unchanged (14–16 %).

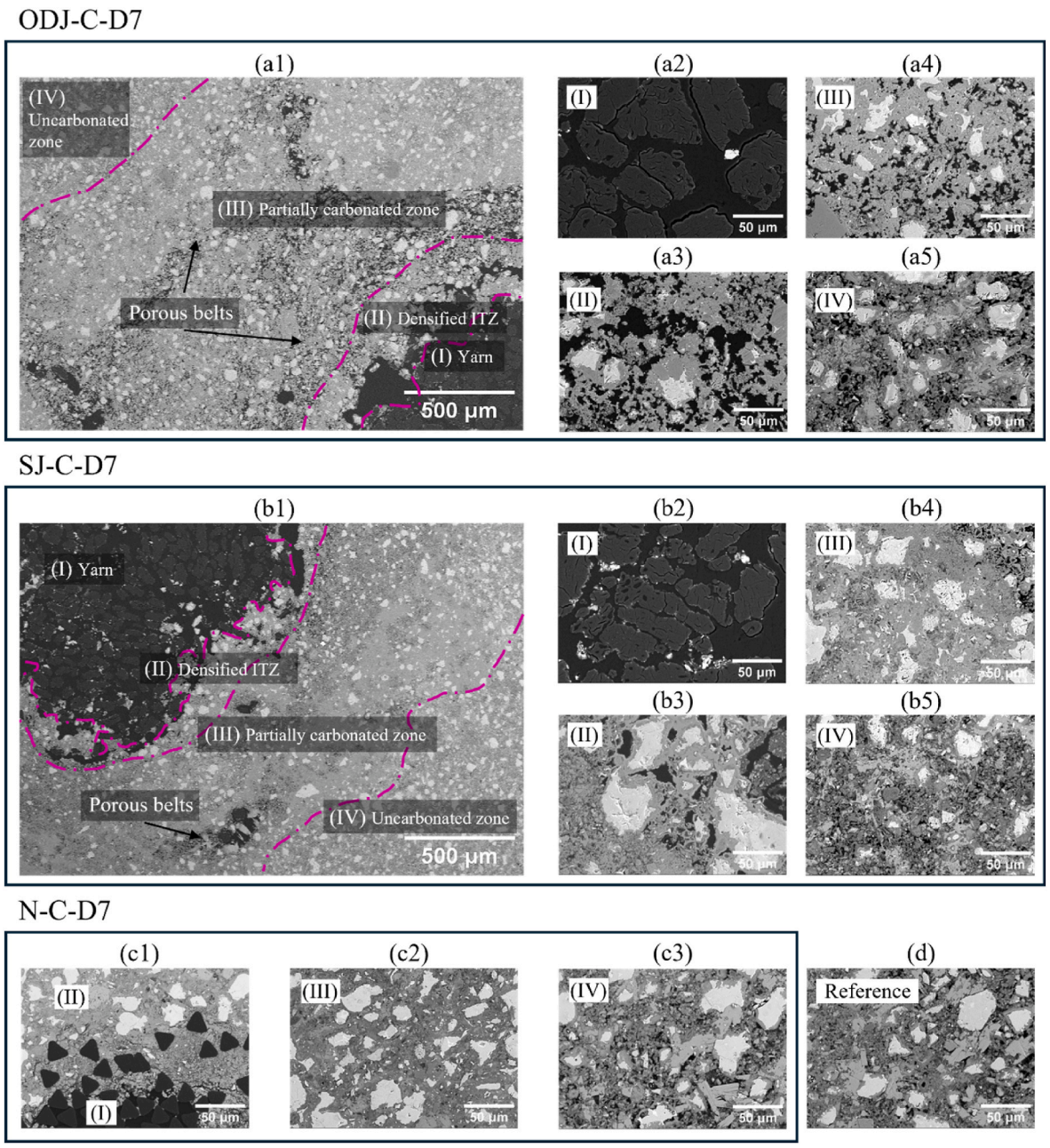


Fig. 8. SEM-BSE images illustrating the microstructural features of yarn–cement paste composites after 7 days of enforced carbonation at 20 mm depth. Four characteristic zones are identified: (I) yarn cross-section; (II) interfacial transition zone (ITZ); (III) porous or partially carbonated matrix; and (IV) uncarbonated matrix. Panels (a1–a5): ODJ-C-D7, showing an (a1) overview at 200× and (a2–a5) corresponding Zones I–IV at 500×. Panels (b1–b5): SJ-C-D7, with (b1) overview and (b2–b5) corresponding Zones I–IV. Panels (c1–c3): N-C-D7, showing Zones I–III. (d) Carbonated reference paste at zone IV.

Across all systems, carbonation effects were mainly confined to the yarn-adjacent region. The outer matrix retained baseline porosity (~15–16 %), comparable to uncarbonated paste. The total modified region extended to approximately 1.2–1.7 mm in jute composites but only ~1.1 mm in nylon, indicating that natural yarns promoted greater local carbonation-induced restructuring of the matrix (Fig. S5). No visible degradation of jute fibres was observed after 7 days of enforced carbonation under the curing conditions examined.

3.4. Compressive strength

Compressive strength increased with curing duration under both air and carbonation regimes (Fig. 9a–c). Carbonation curing produced faster strength gain, particularly between 3 and 7 days, consistent with carbonate formation and matrix densification described in Sections 3.1–3.3. At 7 days, the magnitude of improvement depended on yarn type and yarn volume fraction (i.e. replacement level).

For SJ cement paste composites, carbonation increased 7-day strength from 46.3 MPa to 61.0 MPa (+32 %) in 10–2L (1.52 vol %) and from 42.7 MPa to 55.4 MPa (+30 %) in 5–2L (4.57 vol %). ODJ composites showed smaller but consistent gains, increasing from 53.9 MPa to 63.5 MPa (+18 %) in 10-2L, and from 41.8 MPa to 52.4 MPa (+25 %) in 5-2L configurations. Nylon exhibited a more variable response, with 7-day carbonation increasing strength by +29.6 % in 10–1L and +23.5 % in 5–1L, but only +5–6 % in 2L meshes. Across fibre types, the largest relative gains under carbonation were therefore observed at low to moderate fibre volumes.

The influence of yarn replacement level, governed by yarn spacing

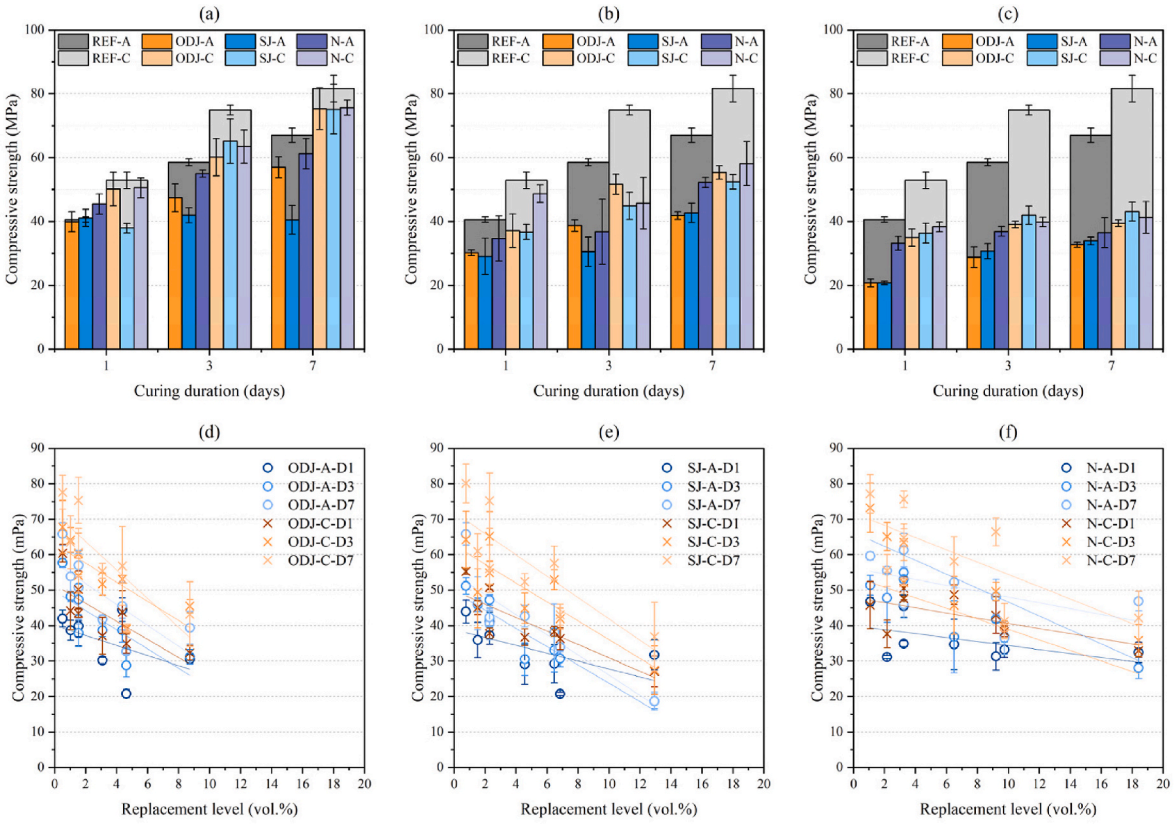


Fig. 9. Compressive strength of yarn–cement paste composites as a function of fibre type, curing regime, curing duration, and fibre volume. (a–c) Strength development at 1, 3, and 7 days for oven-dried jute (ODJ), saturated jute (SJ), and nylon (N) composites under air and carbonation curing, using (a) 5-1L, (b) 5-2L, and (c) 5-3L mesh configurations. (d–f) Compressive strength variation with fibre volume fraction (replacement level) for (d) ODJ, (e) SJ, and (f) N composites at 1, 3, and 7 days, under both curing regimes. Error bars represent ± standard error of the mean (n = 3). Linear trendlines are included for visual reference.

and layer number, is shown in Fig. 9d–f. Strength decreased systematically with increasing yarn content under both curing regimes. Under air curing, increasing from 1L to 2L at 5 mm spacing reduced strength by 10–15 MPa, with a further 5–10 MPa loss for 3L meshes. Under carbonation curing, the reduction from 1L to 2L was larger, typically 20–30 MPa. At low yarn replacement levels (0.76–2.28 vol%), SJ 10–1L and SJ 5–1L reached 80.1 and 75.2 MPa, respectively, comparable to the paste control (77.2 MPa) within experimental scatter. Configurations with 2.5 mm spacing showed the lowest strengths and largest scatter, due to excessive yarn content and poor paste continuity (Supporting Information S1, Section S5). These configurations were not pursued further because the effective carbonation radius (~2–3 mm; Fig. 6d) indicates that such close spacing would produce overlapping carbonation zones and offer limited insight into yarn-controlled transport behaviour. Overall, carbonation-induced densification compensated for yarn-induced defects only at low yarn volume fractions; at higher volume fractions, loss of matrix continuity and increased interfacial volume dominated the mechanical response.

Differences in absolute compressive strength among fibre types at a given yarn volume and curing condition were generally modest and often comparable to the associated standard errors, typically ≤5 MPa for 1L configurations. Therefore, fibre-type differences should be interpreted cautiously where error bars overlap. Under air curing, ODJ showed slightly higher baseline strength (65.8 MPa in 10–1L) than nylon (59.6 MPa) and SJ (57.8 MPa). After carbonation, the strengths of SJ, ODJ, and nylon converged to ~75–80 MPa at low yarn volume fractions. At higher yarn volumes, nylon retained marginally higher absolute strength, but its relative carbonation benefit was smaller.

Overall, compressive strength was controlled primarily by yarn replacement level and curing regime. Among the systems examined, pre-saturated jute showed the largest relative strength gains under carbonation curing at low to moderate fibre volumes, with low variability across replicates in single-layer configurations, distinguishing it from oven-dried jute and synthetic fibres.

4. Discussion

4.1. Hydration and carbonation mechanisms in yarn-cement paste composites

Hydration and carbonation are often treated as competing processes because both depend on pore water and overlapping ionic pathways. Hydration consumes water and generates portlandite and C–S–H, while carbonation proceeds when dissolved CO_2 reacts with Ca^{2+} to form $CaCO_3$. Their relative progression is therefore governed by moisture availability: high pore saturation restricts CO_2 diffusion, while insufficient moisture limits CO_2 dissolution and ion transport [14–16].

In yarn–cement paste composites, the fibre moisture state modifies this balance locally. Pre-saturated jute (SJ) retained moisture near the yarn–matrix interface, supporting CO_2 ingress, dissolution, and ionic mobility. This does not imply unrestricted hydration under the curing conditions (1–7 days, ~20 % CO_2, 64 % RH). Rather, SJ appears to support limited ongoing hydration and clinker dissolution while carbonation remains the dominant reaction, producing progressive CH depletion, $CaCO_3$ accumulation, and local interfacial densification. In contrast, oven-dried jute (ODJ) lacks this moisture-buffering effect; its dry and irregular pore structure may permit gas entry but provides less favourable conditions for CO_2 dissolution, resulting in shallower and less uniform carbonation. Isothermal calorimetry showed only minor differences in bulk hydration kinetics, and XRD confirmed comparable

overall hydration extent across fibre types. The carbonation differences therefore arise mainly from local moisture distribution and yarn-adjacent microstructure, rather than accelerated bulk hydration. This is further supported by the molar-based carbonation index, which was higher for SJ (~0.47) than ODJ (~0.27) at 10 mm depth after 7 days.

These findings point to a revised mechanistic framework, building on prior work that emphasised the trade-off between hydration and carbonation under limited or excessive moisture conditions [9,10,17]. While excessive moisture is known to hinder carbonation, this study shows that localised, retained moisture within embedded yarns can sustain carbonation without blocking gas transport. Although the chamber RH was fixed at 64 %, the yarns created different internal microenvironments. SJ retained and gradually released water along the fibre–matrix interface, maintaining local ion mobility and CO_2 solubility. This enabled a locally coupled hydration–carbonation process in which residual hydration and clinker dissolution could supply Ca^{2+}, while carbonate precipitation remained the dominant sink for Ca-bearing species. In addition to portlandite carbonation, partial C–S–H decalcification likely contributed to the broad low-temperature carbonate decomposition observed in DTG, especially near the CO_2-exposed surface. Synthetic yarns, although porous at the bundle scale, consist of solid polymer filaments without lumen-type internal porosity. Their lower hygroscopicity and limited water storage made them less effective in sustaining moisture-assisted carbonation. Carbonation performance therefore depends not on porosity alone, but on the scale, accessibility, and water-retention capacity of the pore structure.

The mechanistic interpretation is necessarily bounded by the experimental design, which used a single paste composition (CEM I 52.5 N, w/c = 0.40) and one curing regime (~20 % CO_2, 64 % RH, 25 °C). Changes in w/c ratio, binder composition, CO_2 concentration, RH, or exposure duration could modify the balance between hydration, carbonation, and transport. The findings should therefore be read as a mechanistic reference for yarn-assisted early-age carbonation under controlled conditions, rather than as a general model for all cementitious systems.

4.2. Microstructural and quantitative influence of yarn properties on carbonation

Carbonation curing produced distinctive, radially graded microstructures around embedded yarns. This heterogeneous architecture governs how CO_2 and moisture move through the paste and, consequently, how carbonation progresses. System with higher initial moisture (i.e. SJ) showed cross-sectional pore arrangements consistent with more favourable moisture retention and CO_2 transport near the yarn.

In ODJ composites, the high ITZ porosity observed after air curing should be interpreted partly as an initial mixing-induced feature rather than a consequence of carbonation. During casting, dry jute acts as a local water sink, drawing part of the mixing water from the adjacent fresh paste. This local reduction in effective w/c can hinder particle packing and early hydrate formation near the yarn, while fibre swelling followed by subsequent drying may further open interfacial gaps. The resulting ITZ therefore starts from a more porous and less continuous baseline (~32.3 %) before carbonation begins. Nevertheless, in oven-dried jute (ODJ) composites, carbonation remains shallow and irregular. The dry and irregular pore structure observed around ODJ appears less favourable for sustained CO_2 dissolution and transport, showing that visible porosity alone does not guarantee effective carbonation. By contrast, saturated jute (SJ) composites develop a narrower but denser ITZ with fewer unhydrated particles and a well-integrated fibre–matrix interface. The surrounding middle rim, although porous, remains partially saturated due to retained fibre moisture during the curing durations studied. This produces a pore arrangement more favourable for CO_2 dissolution and radial carbonation, forming a wider and more spatially uniform carbonated belt than ODJ. Chemical treatments that reduce fibre water uptake, such as alkalisation, silanisation, or hornification, may therefore produce effects similar to oven-dried jute if they reduce internal moisture buffering, making them unsuitable when maximising CO_2 uptake is the primary objective.

Trends in pore area fraction reported here (Supporting Information, Fig. S4) should be interpreted in light of the inherent constraints of SEM–BSE image analysis. Measurements are based on two-dimensional sections and do not capture three-dimensional pore connectivity. The SEM–BSE results are used here as comparative, spatially resolved indicators of local microstructural modification in defined yarn-adjacent regions, including the ITZ, middle rim, and outer matrix, rather than as a full pore-network characterisation. Consequently, terms referring to transport or pore accessibility are used here as interpretations based on cross-sectional microstructural evidence, rather than as direct measurements of connected pore networks, while greyscale overlap between fine pores and low-density hydrates is unavoidable, particularly within the ITZ. Variability is highest in this region, with standard errors of approximately 2.0–2.4 % for air-cured ODJ and SJ and up to ~3.3 % for nylon near the exposed surface. By contrast, the outer matrix shows consistently low variability (standard errors <0.8 %), consistent with minimal microstructural modification away from yarn influence. Despite these constraints, the observed pore refinement (~15–20 %) is substantially larger than the associated uncertainty. When considered together with the phenolphthalein-stained images, TGA and XRD results, these SEM-BSE data support the reported microstructural trends, although they do not directly prove three-dimensional pore connectivity. Direct confirmation would require three-dimensional methods such as X-ray micro-computed tomography or focused ion beam SEM serial sectioning, although quantifying pore-structure differences across the narrow ITZ and carbonation-induced rim regions would remain challenging because these features span only a few hundred micrometres to millimetres and require high spatial resolution over a representative volume. Similarly, the image-derived carbonation metrics should be interpreted as comparative indicators rather than exact measurements of a sharp carbonation front, since carbonation progresses gradually and partially carbonated regions may not be fully resolved by phenolphthalein staining.

These findings extend our previous work showing that carbonation in natural yarn–cement paste composites is governed by fibre morphology and water sorption capacity [51]. Natural yarns such as cotton and wool, though inherently hydrophilic, exhibited minimal carbonation due to their compact structure and limited moisture uptake (<50 %). Similarly, synthetic yarns such as acrylic, nylon, and polypropylene formed dense, well-bonded interfaces but lacked the lumen-type internal porosity and moisture associated with sustained carbonation near the yarn. In these systems, carbonation remained confined to a narrow interfacial zone or was entirely absent, confirming that carbonation efficacy is controlled by the physical capacity of the yarn to retain water and restructure the surrounding matrix into a semi-saturated, permeable pore structure favourable for carbonation.

The behaviour of coated yarns provides further insight by selectively modifying interfacial porosity while preserving or suppressing internal moisture. Cement-slurry-coated yarns (ODMJ and SMJ) demonstrate that extensive carbonation can still occur even when macropores at the interface are suppressed, provided internal moisture and some pore access remain. The high water-to-cement ratio (0.8) of the slurry likely promotes a porous inner rim around the coated yarns, allowing limited moisture-assisted CO_2 diffusion. As a result, carbonations front in these systems are more compact and concentric than the belt-shaped fronts observed in uncoated SJ composites, reflecting a shift from open pore-mediated to rim-confined transport. In contrast, the epoxy-coated jute (EJ) system suppress carbonation through both physical and chemical effects. The continuous coating blocked internal yarn moisture and gas exchange, while the hydrophobic epoxy surface likely reduced wetting by the aqueous pore solution during mixing. This would limit intimate fibre–paste contact, local hydration, and subsequent carbonation reactions at the interface, leading to negligible microstructural

development. This confirms that the carbonation-promoting role of natural fibres depends on their ability to sustain a humid, accessibe pore network rather than on interfacial porosity alone.

Phenolphthalein-based image analysis supports these interpretations. At 10 mm depth, SJ increased the carbonated area fraction by 32 % relative to ODJ, consistent with its higher water absorption (Table 1). EJ showed a 70–80 % reduction compared with SJ, indicating that interface sealing strongly limits carbonation despite the natural-fibre core. Slurry coatings showed a conditional response: they enhanced carbonation by 3–4 % when applied to ODJ, but reduced it by 44 % when applied to SJ, suggesting that a densified interface can hinder CO_2 transport in moisture-rich conditions. Across all systems, compact synthetic yarns showed 80–85 % lower carbonated area fraction than porous natural yarns, while fibre diameter showed no systematic influence.

Of the scalar parameters assessed, 24-h water absorption was the strongest predictor of carbonation performance. When the depth-averaged effective carbonation radius from 10 to 40 mm after 7 days of carbonation curing was plotted against the 24 h water absorption of the tested yarns, the correlation coefficient reached $R^2 = 0.872$ (Fig. 10). The 95 % confidence band indicates limited scatter around the fitted relationship within the range of yarn absorption values examined, despite the small number of yarn types tested (n = 8). This relationship should, however, be interpreted within the scope of the present study. The yarns were tested at relatively low fibre volume fractions and under a single enforced carbonation regime; at higher yarn contents, where carbonation influence zones overlap, or under different curing durations and humidity conditions, the linear relationship with water absorption may weaken or deviate. By comparison, yarn compactness and diameter showed weaker and less consistent associations with effective carbonation radius. Although high compactness (e.g. in nylon) corresponded with lower carbonation, it was not predictive across yarn types. The lower variability in image-based carbonation analysis compared with our previous work [51] is likely due to improved control of yarn moisture state, which reduced uncertainty in carbonation front delineation.

Overall, these observations affirm that it is not porosity per se, but by the saturation state and accessible pore network around the yarn. The middle rim zone observed under SEM-BSE plays a pivotal role: when semi-saturated and capillary-connected, it becomes a carbonation corridor; when dry, dense, or sealed, it becomes a barrier.

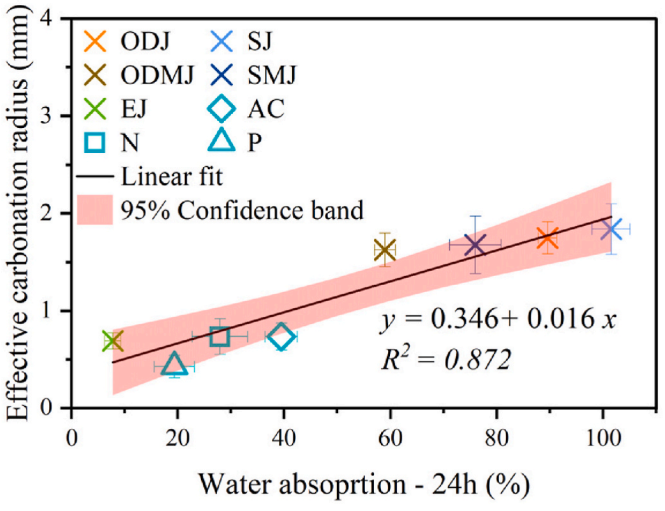


Fig. 10. Relationship between water absorption (24h) of the yarn and depth-averaged effective carbonation radius (10 – 40 mm), after 7 days of enforced carbonation curing.

4.3. Early-age mechanical performance, design limits, and durability implications

The mechanical response of yarn-reinforced cement paste composites under carbonation curing reflects a balance between carbonation-induced matrix densification and the adverse effects of yarn inclusion. It is therefore governed not simply by carbonation depth, but by whether microstructural refinement can compensate for fibre-induced heterogeneity. This balance depends on fibre morphology, internal moisture availability, and spatial arrangement within the matrix. Porous, twisted natural yarns generate more interfacial complexity than compact synthetic filaments, but also offer greater potential for carbonation-induced densification. At low yarn volumes, densification of the ITZ and adjacent matrix can offset fibre-induced heterogeneity and preserve compressive strength. At higher yarn volumes, the reduced load-bearing paste fraction and cumulative extent of interfacial and porous rim regions dominate, so greater carbonation extent does not translate directly into higher strength.

It should be noted that the mechanical assessment is limited to compressive strength. This test is sensitive to matrix continuity, porosity, and carbonation-induced densification, but it does not directly capture the main reinforcing functions of yarns, such as crack bridging, pull-out resistance, fracture energy, or post-cracking behaviour. Therefore, the mechanical results should be interpreted as evidence of early-age compressive strength retention, not as a full assessment of yarn–matrix mechanical interaction. Flexural, tensile, and fracture-based tests are required to evaluate the contribution of yarns to post-cracking performance.

Within this framework, SJ composites demonstrate that moisture-buffered yarns can recover fibre-related strength loss while enabling higher CO_2 uptake. Among the tested system, the threshold for reliable strength recovery was observed below approximately 2.3 vol% yarn replacement. This is notably higher than typical fibre contents in engineered cementitious composites systems, where common cellulose dosages range from 0.2 to 1.5 vol% by binder volume [47,74,75].

These outcomes provide direct guidance for designing and applying yarn–cement paste composites in CO_2-curable systems, and are most readily aligned with precast or factory-based production where CO_2 concentration, relative humidity, and curing duration can be regulated. Single-layer saturated jute (SJ) meshes with 5–10 mm spacing and approximately 0.8 vol% fibre (10–1L) achieved the best balance between CO_2 uptake and compressive strength, making them suitable for thin-section elements such as façade panels, precast blocks, and modular wall units where reinforcement volume must remain low [76]. Higher-volume configurations, including 5–1L and multi-layer (2–3L) meshes, may be more appropriate for non-structural or repair applications requiring enhanced durability, crack control, or deformation tolerance rather than peak strength [77]. Because the yarns are placed rather than mixed, the concept functions as a reinforcement and transport scaffold, analogous in implementation to textile-reinforced mortars; this approach decouples reinforcement from paste rheology and eliminates the need for high flowability or chemical admixtures. Yarn placement can be achieved using manual positioning, prefabricated meshes, or textile inserts, and is compatible with automated mould-based or robotic assembly processes commonly used in precast manufacturing.

From a materials selection perspective, simple pre-saturation is sufficient to sustain carbonation and promote interfacial densification, whereas complex coatings like cement slurry layers offer only marginal benefit in already saturated systems and can be omitted unless surface protection is required under dry or aggressive conditions. From a practical perspective, the slurry coating is therefore not recommended for saturated jute when the primary objective is to maximise CO_2 uptake. Although it may create a more defined interfacial rim, it reduces the carbonation benefit provided by the open, moisture-retentive structure of SJ. Fibre selection should therefore prioritise high water absorption

capacity and moderate compactness when early-age carbonation efficiency and strength development are the primary objectives. Furthermore, the strong correlation between effective carbonation radius (from image analysis) and CO_2 uptake offers a practical means to screen yarn types for carbonation performance without extensive thermogravimetric testing (Fig. 6d).

Furthermore, while this study focused on cement paste to isolate fibre-related effects, extension to mortar or concrete systems will require the incorporation of fine aggregates that may alter fibre–matrix interactions and CO_2 transport pathways, requiring further evaluation under more representative material systems and casting conditions.

Beyond early-age performance, the continuous porous architecture of natural yarns raises durability concerns. The yarn-induced pore network can act as a preferential pathway for capillary water and dissolved ions, shifting durability control from bulk paste permeability to transport along fibre-adjacent corridors. In natural fibre yarn-reinforced composites, this network facilitates Ca^{2+} ingress into fibre lumens and cell walls, promoting mineralisation and degradation of fibre–matrix bonding [78,79]. Carbonation curing may partially mitigate this process by consuming portlandite and lowering pore-solution alkalinity near the yarns [38]. Once the carbonation front stabilises, the local environment around saturated jute is expected to be less alkaline and more carbonate-rich than in uncarbonated natural fibre–cement systems. This may slow alkaline hydrolysis and mineralisation of the jute cell wall, while carbonate precipitation at the interface may reduce direct exposure of the fibre to portlandite-rich pore solution. However, this possible protective effect does not remove the durability risk, because the same lumen and inter-filament void structure that promotes early CO_2 transport may later facilitate moisture ingress and ion transport under wetting–drying exposure. This issue is particularly relevant for thin-section elements, where yarns may lie close to exposed surfaces and the transport distance from the environment is short. No fibre degradation was observed over 1–7 days in this study, however, this duration is insufficient to assess long-term stability under sustained moisture ingress or cyclic environmental exposure, which could thus be considered in future research.

These mechanisms have direct implications for carbonation-compatible composite design. Fibre treatments commonly used to improve durability in natural fibre composites, which reduce fibre hydrophilicity [80], are unsuitable when applied before carbonation curing because they suppress the moisture buffering needed to sustain carbonation at depth. Durability control in yarn-reinforced systems could therefore be implemented after carbonation, targeting yarn-induced internal transport pathways while preserving the carbonated microstructure. Conventional post-curing strategies such as surface hydrophobisation, inorganic pore blocking, polymer-modified coatings, recast layers, or dense organic barriers mainly affect near-surface paste transport and do not address the millimetre-scale, continuous pathways created by yarns [81,82]. A more compatible approach is near-surface impregnation with low-viscosity organic or organo-silicate systems (e.g. epoxy, polyurethane, alkoxysilane-based resins) [83–85], applied after carbonation curing and controlled drying. When directed at surfaces where yarn corridors are exposed, such treatments could infiltrate connected yarn and interfacial pores by capillary suction, potentially assisted by mild vacuum or pressure, and then partially occlude internal transport paths after solidification.

Overall, the results support a staged approach: carbonation curing to exploit yarn-enhanced CO_2 transport and early-age strength recovery, followed by post-curing interventions that restrict further access to yarn-induced transport pathways. Although long-term durability is not assessed here, the mechanisms identified set clear priorities for future work, including extended exposure tests, wet–dry cycling, and evaluation of fibre–matrix bond stability after post-carbonation protection.

5. Conclusions

This study demonstrates that under enforced carbonation (~20 vol% CO_2, 64 % RH, 25 °C), the early-age behaviour of yarn–cement pastes is controlled not by fibre type alone but by how the fibre modifies pore connectivity, moisture retention, and interfacial transport property. Saturated jute yarns enabled the deepest and most uniform carbonation, its lumina acting as distributed moisture reservoirs that sustained CO_2 dissolution and promote interfacial densification. In contrast, synthetic and epoxy-coated fibres, characterised by compact or sealed architectures, restricted moisture exchange and exhibited negligible carbonation engagement. Pre-saturation alone proved sufficient to activate strong fibre–matrix interaction, while additional surface treatments such as cement slurry coatings provided limited benefit under moist conditions. Across systems, yarn water absorption correlated closely with carbonation depth and uptake, establishing a practical selection metric for CO_2-compatible composites.

The concept of an effective carbonation radius provides a quantitative basis for selecting yarn spacing in mesh-reinforced systems, supporting efficient spatial deployment of carbonation influence zones without excessive overlap. Overall, fibres that generate semi-saturated and accessible pore structures near the interface can shift carbonation from a surface-limited reaction towards a more matrix-integrated process, improving CO_2 uptake while preserving early-age compressive strength only at low yarn volumes. While this study focuses on early-age behaviour, the mechanisms identified indicate that control of yarn-induced transport pathways will be central to long-term durability, warranting future investigation under sustained moisture ingress and cyclic exposure.

CRediT authorship contribution statement

Yixiu Zhuge: Formal analysis, Investigation, Methodology, Writing – original draft. **Hong S. Wong:** Supervision, Visualization, Writing – review & editing. **Rupert J. Myers:** Conceptualization, Funding acquisition, Supervision, Visualization, Writing – review & editing.

Declaration of competing interest

The authors declare that they have no known competing financial interests or personal relationships that could have appeared to influence the work reported in this paper.

Acknowledgements

The research leading to this publication benefitted from EPSRC funding under grant Nos. EP/R010161/1 and EP/Y001370/1 (selected by the European Research Council (ERC) for a Starting Grant, funded by the EPSRC Frontier Research Guarantee), and from support from the UKCRIC Coordination Node, EPSRC grant number EP/R017727/1, which funds UKCRIC's ongoing coordination. The authors would like to thank Pei Boon Ong for assistance with image analysis, and Jianhang Feng for technical support and general discussions.

Appendix A. Supplementary data

Supplementary data to this article can be found online at https://doi.org/10.1016/j.cemconcomp.2026.106737.

Data availability

Data will be made available on request.

References

[1] S.A. Miller, M. Juenger, K.E. Kurtis, J. Weiss, Cement and alternatives in the Anthropocene, Annu. Rev. Environ. Resour. 49 (2024) 309–335, https://doi.org/10.1146/annurev-environ-112621-070104.

[2] International Energy Agency (IEA), Cement Tracking Report, IEA, Paris, 2021.

[3] S. Wu, Z. Shao, R.M. Andrew, L. Bing, J. Wang, L. Niu, Z. Liu, F. Xi, Global CO_2 uptake by cement materials from 1930 to 2023, Sci. Data 11 (2024) 1–11, https://doi.org/10.1038/s41597-024-04234-8.

[4] L. Niu, S. Wu, R.M. Andrew, Z. Shao, J. Wang, F. Xi, Global and national CO_2 uptake by cement carbonation from 1928 to 2024, Earth Syst. Sci. Data 17 (2025) 2231–2247, https://doi.org/10.5194/essd-17-2231-2025.

[5] R. Guo, J. Wang, L. Bing, D. Tong, P. Ciais, S.J. Davis, R.M. Andrew, F. Xi, Z. Liu, Global CO_2 uptake by cement from 1930 to 2019, Earth Syst. Sci. Data 13 (2021) 1791–1805, https://doi.org/10.5194/essd-13-1791-2021.

[6] J.G. Driver, E. Bernard, P. Patrizio, P.S. Fennell, K. Scrivener, R.J. Myers, Global decarbonization potential of CO_2 mineralization in concrete materials, Proc. Natl. Acad. Sci. U. S. A. 121 (2024) e2313475121, https://doi.org/10.1073/pnas.2313475121.

[7] S. Pamenter, R.J. Myers, Decarbonizing the cementitious materials cycle: a whole-systems review of measures to decarbonize the cement supply chain in the UK and European contexts, J. Ind. Ecol. 25 (2021) 359–376, https://doi.org/10.1111/jiec.13105.

[8] N. Thonemann, L. Zacharopoulos, F. Fromme, J. Nühlen, Environmental impacts of carbon capture and utilization by mineral carbonation: a systematic literature review and meta life cycle assessment, J. Clean. Prod. 332 (2022) 130067, https://doi.org/10.1016/j.jclepro.2021.130067.

[9] D. Zhang, Z. Ghouleh, Y. Shao, Review on carbonation curing of cement-based materials, J. CO_2 Util. 21 (2017) 119–131, https://doi.org/10.1016/j.jcou.2017.07.003.

[10] Z. Liu, W. Meng, Fundamental understanding of carbonation curing and durability of carbonation-cured cement-based composites: a review, J. CO_2 Util. 44 (2021) 101428, https://doi.org/10.1016/j.jcou.2020.101428.

[11] Z. Zhang, K. Zheng, L. Chen, Q. Yuan, Review on accelerated carbonation of calcium-bearing minerals: carbonation behaviours, reaction kinetics, and efficiency improvement, J. Build. Eng. 86 (2024) 108826, https://doi.org/10.1016/j.jobe.2024.108826.

[12] B. Lu, S. Drissi, J. Liu, X. Hu, B. Song, C. Shi, Effect of temperature on CO_2 curing, compressive strength and microstructure of cement paste, Cement Concr. Res. 157 (2022) 106827, https://doi.org/10.1016/j.cemconres.2022.106827.

[13] M. Zajac, H. Hilbig, F. Bullerjahn, M. Ben Haha, Reactions involved in carbonation hardening of Portland cement: effect of curing temperature, J. Sustain. Cem. Based Mater. 12 (2023) 1107–1125, https://doi.org/10.1080/21650373.2022.2163432.

[14] A. Vollpracht, G.J.G. Gluth, B. Rogiers, I.D. Uwanuakwa, Q.T. Phung, Y. Villagran Zaccardi, C. Thiel, H. Vanoutrive, J.M. Etcheverry, E. Gruyaert, S. Kamali-Bernard, A. Kanellopoulos, Z. Zhao, I.M. Martins, S. Rathnarajan, N. De Belie, Report of RILEM TC 281-CCC: insights into factors affecting the carbonation rate of concrete with SCMs revealed from data mining and machine learning approaches, Mater. Struct. 57 (2024) 1–33, https://doi.org/10.1617/s11527-024-02465-0.

[15] S. von Greve-Dierfeld, B. Lothenbach, A. Vollpracht, B. Wu, B. Huet, C. Andrade, C. Medina, C. Thiel, E. Gruyaert, H. Vanoutrive, I.F. Saéz del Bosque, I. Ignjatovic, J. Elsen, J.L. Provis, K. Scrivener, K.-C. Thienel, K. Sideris, M. Zajac, N. Alderete, Ö. Cizer, P. Van den Heede, R.D. Hooton, S. Kamali-Bernard, S.A. Bernal, Z. Zhao, Z. Shi, N. De Belie, Understanding the carbonation of concrete with supplementary cementitious materials: a critical review by RILEM TC 281-CCC, Mater. Struct. 53 (2020) 136, https://doi.org/10.1617/s11527-020-01558-w.

[16] R.H. Filomeno, L.B. Rodier, J.E.M. Ballesteros, J.A. Rossignolo, H. Savastano, Optimizing the modified atmosphere parameters in the carbonation process for improved fibre–cement performance, J. Build. Eng. 32 (2020) 101676, https://doi.org/10.1016/j.jobe.2020.101676.

[17] G. Liyew, N. Lee, S. Park, H.K. Lee, J.J. Park, H.K. Kim, Understanding mechanisms of carbonation curing for Portland cement through phase profiling via QXRD analysis and thermodynamic modeling, J. CO_2 Util. 87 (2024) 102919, https://doi.org/10.1016/j.jcou.2024.102919.

[18] I.E. Teune, K. Schollbach, M.V.A. Florea, H.J.H. Brouwers, Carbonation of hydrated cement: the impact of carbonation conditions on CO_2 sequestration, phase formation, and reactivity, J. Build. Eng. 79 (2023) 107785, https://doi.org/10.1016/j.jobe.2023.107785.

[19] D. Zhang, V.C. Li, B.R. Ellis, Optimal pre-hydration age for CO_2 sequestration through Portland cement carbonation, ACS Sustain. Chem. Eng. 6 (2018) 15976–15981, https://doi.org/10.1021/acssuschemeng.8b03699.

[20] P. Xin, H. Liu, J. Wang, Y. Wang, H. Wang, S. Cui, Effects of CO_2-absorbed triethanolamine solutions on strength development of cement mortars and the mechanism: synergism of cement hydration and carbonation, Constr. Build. Mater. 413 (2024) 134708, https://doi.org/10.1016/j.conbuildmat.2023.134708.

[21] S.K. Saikia, A.S. Rajput, Effect of carbon sequestration methods on uptake potential and characteristics of ordinary Portland cement-based concrete, Constr. Build. Mater. 418 (2024) 135330, https://doi.org/10.1016/j.conbuildmat.2024.135330.

[22] C. Li, Y. Li, W. Zhu, G. Zeng, Z. Ouyang, M. Cheng, Z. Jiang, Carbon dioxide-cured building materials as an approach to decarbonizing the calcium carbide-related industry, Renew. Sustain. Energy Rev. 186 (2023) 113688, https://doi.org/10.1016/j.rser.2023.113688.

[23] A.K. Shuvo, P.K. Sarker, F.U.A. Shaikh, Efficacy of various accelerated carbonation techniques to improve recycled concrete aggregates: a comprehensive review, J. Build. Eng. 95 (2024) 110257, https://doi.org/10.1016/j.jobe.2024.110257.

[24] C. Liang, B. Li, M.Z. Guo, S. Hou, S. Wang, Y. Gao, X. Wang, Effects of early-age carbonation curing on the properties of cement-based materials: a review, J. Build. Eng. 84 (2024) 108495, https://doi.org/10.1016/j.jobe.2024.108495.

[25] C. Liu, J. Wang, C. Yu, Y. Kong, Z. Hu, J. Liu, Carbonation strengthening mechanism of dry cement-based materials under supercritical carbon dioxide, J. Build. Eng. 94 (2024) 109915, https://doi.org/10.1016/j.jobe.2024.109915.

[26] S. Chu, R.T. Rashid, Y. Pan, X. Wang, H. Zhang, R. Xiao, Impact of flue gas impurities and concentrations on photoelectrochemical CO_2 reduction, J. CO_2 Util. 60 (2022) 101993, https://doi.org/10.1016/j.jcou.2022.101993.

[27] Z. He, S. Wang, M. Mahoutian, Y. Shao, Flue gas carbonation of cement-based building products, J. CO_2 Util. 37 (2020) 309–319, https://doi.org/10.1016/j.jcou.2020.01.001.

[28] X. Xian, D. Zhang, Y. Shao, Flue gas carbonation curing of cement paste and concrete at ambient pressure, J. Clean. Prod. 313 (2021) 127943, https://doi.org/10.1016/j.jclepro.2021.127943.

[29] T. Higuchi, M. Morioka, I. Yoshioka, K. Yokozeki, Development of a new ecological concrete with CO_2 emissions below zero, Constr. Build. Mater. 67 (2014) 338–343, https://doi.org/10.1016/j.conbuildmat.2014.01.029.

[30] S. Liu, P. Shen, D. Xuan, L. Li, A. Sojobi, B. Zhan, C.S. Poon, Comparison of liquid–solid and gas–solid accelerated carbonation for enhancement of recycled concrete aggregate, Cem. Concr. Compos. 118 (2021) 103988, https://doi.org/10.1016/j.cemconcomp.2021.103988.

[31] H. El-Hassan, Y. Shao, Z. Ghouleh, Effect of initial curing on carbonation of lightweight concrete masonry units, ACI Mater. J. 110 (2013) 441–450, https://doi.org/10.14359/51685791.

[32] T.P. Hills, F. Gordon, N.H. Florin, P.S. Fennell, Statistical analysis of the carbonation rate of concrete, Cement Concr. Res. 72 (2015) 98–107, https://doi.org/10.1016/j.cemconres.2015.02.007.

[33] E. Van Roijen, K. Sethares, A. Kendall, S.A. Miller, The climate benefits from cement carbonation are being overestimated, Nat. Commun. 15 (2024) 1–11, https://doi.org/10.1038/s41467-024-48965-z.

[34] H. Bao, G. Xu, M. Yu, Q. Wang, R. Li, M. Saafi, J. Ye, Evolution of the ITZ and its effect on carbonation depth of concrete under supercritical CO_2 conditions, Cem. Concr. Compos. 126 (2022) 104336, https://doi.org/10.1016/j.cemconcomp.2021.104336.

[35] R. Hay, P. Krishnan, K. Celik, Influence of natural fibres on hydration and carbonation of reactive magnesium oxide cement, Constr. Build. Mater. 411 (2024) 134653, https://doi.org/10.1016/j.conbuildmat.2023.134653.

[36] S.F. Santos, R. Schmidt, A.E.F.S. Almeida, G.H.D. Tonoli, H. Savastano, Supercritical carbonation treatment of extruded fibre–cement composites reinforced with vegetable fibres, Cem. Concr. Compos. 56 (2015) 84–94, https://doi.org/10.1016/j.cemconcomp.2014.11.007.

[37] G.H.D. Tonoli, V.D. Pizzol, G. Urrea, S.F. Santos, L.M. Mendes, V. Santos, V. M. John, M. Frías, H. Savastano, Rationalizing the impact of ageing on the fibre–matrix interface and stability of cement-based composites subjected to early-age carbonation, J. Mater. Sci. 51 (2016) 7929–7943, https://doi.org/10.1007/s10853-016-0060-z.

[38] G.H.D. Tonoli, S.F. Santos, A.P. Joaquim, H. Savastano, Effect of accelerated carbonation on cementitious roofing tiles reinforced with lignocellulosic fibre, Constr. Build. Mater. 24 (2010) 193–201, https://doi.org/10.1016/j.conbuildmat.2007.11.018.

[39] M. Hou, Z. Li, V.C. Li, Green and durable engineered cementitious composites with recycled PE fibre, desert sand, and carbonation curing: mixture design, durability performance, and life-cycle analysis, Constr. Build. Mater. 414 (2024) 134984, https://doi.org/10.1016/j.conbuildmat.2024.134984.

[40] L. Hu, Y. Yao, C. Liu, J. Sun, W. Li, H. Yang, G. He, F. Yuan, Comparative study of dynamic mechanical properties and carbonation–hydration kinetics of CO_2-cured high-performance cementitious composites, Cem. Concr. Compos. 143 (2023) 105227, https://doi.org/10.1016/j.cemconcomp.2023.105227.

[41] W.H. Hu, D. Zhang, E. Ftwi, B.R. Ellis, V.C. Li, Development of sustainable low-carbon engineered cementitious composites with waste polyethylene fibre, sisal fibre and carbonation curing, Resour. Conserv. Recycl. 197 (2023) 107096, https://doi.org/10.1016/j.resconrec.2023.107096.

[42] P. Jongvisuttisun, C. Negrello, K.E. Kurtis, Effect of processing variables on efficiency of eucalyptus pulps for internal curing, Cem. Concr. Compos. 37 (2013) 126–135, https://doi.org/10.1016/j.cemconcomp.2012.11.006.

[43] P. Jongvisuttisun, J. Leisen, K.E. Kurtis, Key mechanisms controlling internal curing performance of natural fibres, Cement Concr. Res. 107 (2018) 206–220, https://doi.org/10.1016/j.cemconres.2018.02.007.

[44] M. Miyauchi, Water adsorption on hydrophilic fibres and porous and deliquescent materials: cellulose, polysaccharides, silica, inorganic salts, sugar alcohols and amino acids, ACS Omega 8 (2023) 44212–44220, https://doi.org/10.1021/acsomega.3c06642.

[45] A. Baltazar-y-Jimenez, A. Bismarck, Wetting behaviour, moisture uptake and electrokinetic properties of lignocellulosic fibres, Cellulose 14 (2007) 115–127, https://doi.org/10.1007/s10570-006-9092-x.

[46] K. Liu, J. Yu, Y. Chen, Z. Zhang, C. Mei, H. Liu, G. Yang, X. Zhang, Preparation of cellulose fibre sheets and their impact on pore connectivity of cement paste during early hydration, Constr. Build. Mater. 411 (2024) 134535, https://doi.org/10.1016/j.conbuildmat.2023.134535.

[47] S. Feng, J. Lyu, H. Xiao, J. Feng, Application of cellulose fibre in ultra-high-performance concrete to mitigate autogenous shrinkage, J. Sustain. Cem. Based Mater. 12 (2023) 842–855, https://doi.org/10.1080/21650373.2022.2119618.

[48] C.H. Yeh, J.H. Wu, T.C. Yang, Drying shrinkage and mechanical strength of cementitious composites with alkali-treated Makino bamboo fibres, J. Nat. Fibers 21 (2024) 1–12, https://doi.org/10.1080/15440478.2024.2321531.

[49] E.M. Ernest, A.C. Peter, Application of selected chemical modification agents on banana fibre for enhanced composite production, Clean. Mater. 5 (2022) 100131, https://doi.org/10.1016/j.clema.2022.100131.
[50] M. Fei, W. Fu, X. Zheng, Y. Chen, W. Liu, R. Qiu, Enhancing cement composite interfaces with waterglass modification of bamboo fibres, Constr. Build. Mater. 411 (2024) 134338, https://doi.org/10.1016/j.conbuildmat.2023.134338.
[51] Y. Zhuge, P.B. Ong, H.S. Wong, R.J. Myers, Natural fibre-enhanced CO_2 transport and uptake in cement pastes subjected to enforced carbonation, J. CO_2 Util. 90 (2024) 102983, https://doi.org/10.1016/j.jcou.2024.102983.
[52] S. Roy, L.B. Lutfar, Bast fibres: jute, in: Handbook of Natural Fibres, Elsevier, Oxford, 2012, pp. 39–59, https://doi.org/10.1016/b978-0-12-818398-4.00003-7, 2nd ed., vol. 1.
[53] M.S. Rahman, Jute – a versatile natural fibre: cultivation, extraction and processing, in: Industrial Applications of Natural Fibres: Structure, Properties and Technical Applications, Wiley, Chichester, 2010, pp. 135–161, https://doi.org/10.1002/9780470660324.ch6.
[54] A.K. Singh, The potential of jute crop for mitigation of greenhouse gas emissions in a changing climatic scenario, Int. J. Agric. Sci. 13 (2017) 419–423, https://doi.org/10.15740/has/ijas/13.2/419-423.
[55] T. Sanyal, Jute, jute fibre and jute yarn, in: Jute Geotextiles and their Applications in Civil Engineering, Springer, Singapore, 2017, pp. 7–17, https://doi.org/10.1007/978-981-10-1932-6_2.
[56] J. Ahmad, M.M. Arbili, A. Majdi, F. Althoey, A.F. Deifalla, C. Rahmawati, Performance of concrete reinforced with jute fibres: a review, J. Eng. Fibers Fabrics 17 (2022) 1–17, https://doi.org/10.1177/15589250221121871.
[57] T. Sen, H.N. Jagannatha Reddy, Strengthening of RC beams in flexure using natural jute fibre textile-reinforced composite systems and comparison with CFRP and GFRP strengthening, Int. J. Sustain. Built Environ. 2 (2013) 41–55, https://doi.org/10.1016/j.ijsbe.2013.11.001.
[58] M.A.S. Sujon, M.A. Habib, M.Z. Abedin, Experimental investigation of mechanical and water absorption properties of jute/carbon epoxy hybrid composites with different fibre stacking sequences and orientations, J. Mater. Res. Technol. 9 (2020) 10970–10981, https://doi.org/10.1016/j.jmrt.2020.07.079.
[59] R. Masoodi, K.M. Pillai, Moisture absorption and swelling in bio-based jute–epoxy composites, J. Reinforc. Plast. Compos. 31 (2012) 285–294, https://doi.org/10.1177/0731684411434654.
[60] L.A. Pereira-De-Oliveira, J.P. Castro-Gomes, M.C.S. Nepomuceno, Effect of acrylic fibre geometry on physical, mechanical and durability properties of cement mortars, Constr. Build. Mater. 27 (2012) 189–196, https://doi.org/10.1016/j.conbuildmat.2011.07.061.
[61] S. Spadea, I. Farina, A. Carrafiello, F. Fraternali, Recycled nylon fibres as cement mortar reinforcement, Constr. Build. Mater. 80 (2015) 200–209, https://doi.org/10.1016/j.conbuildmat.2015.01.075.
[62] R.S. Rahbar, S.A.M. Shoushtary, M. Abdouss, A. Khosroushahy, Production and characterisation of multifilament yarns made from polypropylene containing small amounts of oxidised polypropylene, J. Chem. Res. 2006 (2006) 121–126, https://doi.org/10.3184/030823406776330945.
[63] M. Tausif, T. Cassidy, I. Butcher, Yarn and thread manufacturing methods for high-performance apparel, in: High-Performance Apparel: Materials, Development, and Applications, Woodhead Publishing, Oxford, 2018, pp. 33–73, https://doi.org/10.1016/b978-0-08-100904-8.00003-1.
[64] British Standards Institution, Plastics – Determination of Water Absorption, BS EN ISO 62, BSI, London, 2008, https://doi.org/10.3403/30172707.
[65] A. Peled, B. Mobasher, A. Bentur, Textile Reinforced Concrete, CRC Press, Boca Raton, 2017, https://doi.org/10.1201/9781315119151.
[66] R. Snellings, J. Chwast, Ö. Cizer, N. De Belie, Y. Dhandapani, P. Durdzinski, J. Elsen, J. Haufe, D. Hooton, C. Patapy, M. Santhanam, K. Scrivener, D. Snoeck, L. Steger, S. Tongbo, A. Vollpracht, F. Winnefeld, B. Lothenbach, RILEM TC-238 SCM recommendation on hydration stoppage by solvent exchange for the study of hydrate assemblages, Mater. Struct. 51 (2018) 1–4, https://doi.org/10.1617/s11527-018-1298-5.
[67] British Standards Institution, Testing Hardened Concrete – Part 12: Determination of the Carbonation Resistance of Concrete – Accelerated Carbonation Method, BS EN 12390-12, BSI, London, 2020.
[68] H.S. Wong, M.K. Head, N.R. Buenfeld, Pore segmentation of cement-based materials from backscattered electron images, Cement Concr. Res. 36 (2006) 1083–1090, https://doi.org/10.1016/j.cemconres.2005.10.006.
[69] K. Scrivener, R. Snellings, B. Lothenbach, A Practical Guide to Microstructural Analysis of Cementitious Materials, CRC Press, Boca Raton, 2018, https://doi.org/10.1201/b19074.
[70] British Standards Institution, Methods of Testing Cement – Part 11: Heat of Hydration – Isothermal Conduction Calorimetry Method, BS EN 196-11, BSI, London, 2019, https://doi.org/10.3403/30361319U.
[71] H. Mehdizadeh, T.C. Ling, Hydration and strength of cement paste containing metastable vaterite derived from recycled concrete fines and CO_2, Cement Concr. Res. 194 (2025) 107891, https://doi.org/10.1016/j.cemconres.2025.107891.
[72] J. Huang, Y. Chen, Q. Yu, Amorphous calcium carbonate formation from carbonated recycled cement powder: a carbonation-activated cementitious material, Composites, Part B Eng. 297 (2025) 112336, https://doi.org/10.1016/j.compositesb.2025.112336.
[73] X. Chen, S. Li, M. Hu, Y. Geng, S. Meng, L. Jin, Q. Hu, S. Han, Early-age accelerated carbonation of cementitious material surfaces under low CO_2 concentration, Constr. Build. Mater. 445 (2024) 137975, https://doi.org/10.1016/j.conbuildmat.2024.137975.
[74] H. Jamshaid, R.K. Mishra, A. Raza, U. Hussain, M.L. Rahman, S. Nazari, V. Chandan, M. Müller, R. Chotěborský, Natural cellulosic fibre-reinforced concrete: influence of fibre type and loading percentage on mechanical and water absorption performance, Materials 15 (2022) 874, https://doi.org/10.3390/ma15030874.
[75] I.S. Siqueira, R.D.T. Filho, E. Koenders, Influence of cellulose pulp fibre addition on hydration of cementitious pastes with silica fume, in: Proc. Int. Conf. on Building Materials (ICBBM), 2015, https://doi.org/10.26168/icbbm2015.77. Paper 77.
[76] K. Pidun, M. Schulze, Designed textile-reinforced concrete elements for architectural façade applications, Appl. Mech. Mater. 719–720 (2015) 171–176, https://doi.org/10.4028/www.scientific.net/amm.719-720.171.
[77] J. Orlowsky, M. Beßling, V. Kryzhanovskyi, Prospects for the use of textile-reinforced concrete in buildings and structures maintenance, Buildings 13 (2023) 189, https://doi.org/10.3390/buildings13010189.
[78] L.B. Addis, Z.B. Sendekie, N. Satheesh, Degradation kinetics and durability enhancement strategies of cellulosic fibre-reinforced geopolymers and cement composites, Adv. Mater. Sci. Eng. 2022 (2022) 1981755, https://doi.org/10.1155/2022/1981755.
[79] E. Booya, K. Gorospe, H. Ghaednia, S. Das, Durability properties of engineered pulp fibre-reinforced concretes made with and without supplementary cementitious materials, Composites, Part B Eng. 172 (2019) 376–386, https://doi.org/10.1016/j.compositesb.2019.05.070.
[80] L. Prabhu, V. Krishnaraj, S. Sathish, S. Gokulkumar, N. Karthi, L. Rajeshkumar, D. Balaji, N. Vigneshkumar, K.S. Elango, Review of natural fibre-reinforced hybrid composites: chemical treatments, manufacturing methods and potential applications, Mater. Today Proc. 45 (2021) 8080–8085, https://doi.org/10.1016/j.matpr.2021.01.280.
[81] X. Pan, Z. Shi, C. Shi, T.C. Ling, N. Li, Review of concrete surface treatments – part I: types and mechanisms, Constr. Build. Mater. 132 (2017) 578–590, https://doi.org/10.1016/j.conbuildmat.2016.12.025.
[82] X. Pan, Z. Shi, C. Shi, T.C. Ling, N. Li, Review of concrete surface treatments – part II: performance, Constr. Build. Mater. 133 (2017) 81–90, https://doi.org/10.1016/j.conbuildmat.2016.11.128.
[83] G. Batis, P. Pantazopoulou, A. Routoulas, Corrosion protection of reinforcement by inorganic coatings in the presence of alkanolamine-based inhibitors, Cem. Concr. Compos. 25 (2003) 371–377, https://doi.org/10.1016/s0958-9465(02)00061-6.
[84] C. Wu, Y. Pan, L. Yan, Mechanical properties and durability of textile-reinforced concrete: a review, Polymers 15 (2023) 3826, https://doi.org/10.3390/polym15183826.
[85] P. Zhang, F.H. Wittmann, T. Zhao, E.H. Lehmann, Neutron imaging of water penetration into cracked steel-reinforced concrete, Physica B Condens. Matter 405 (2010) 1866–1871, https://doi.org/10.1016/j.physb.2010.01.065.